

Measurement of χ_{cJ} decaying into $\eta'K^+K^-$

M. Ablikim,¹ M. N. Achasov,^{8,a} X. C. Ai,¹ O. Albayrak,⁴ M. Albrecht,³ D. J. Ambrose,⁴¹ F. F. An,¹ Q. An,⁴² J. Z. Bai,¹ R. Baldini Ferroli,^{19a} Y. Ban,²⁸ J. V. Bennett,¹⁸ M. Bertani,^{19a} J. M. Bian,⁴⁰ E. Boger,^{21,b} O. Bondarenko,²² I. Boyko,²¹ S. Braun,³⁷ R. A. Briere,⁴ H. Cai,⁴⁷ X. Cai,¹ O. Cakir,^{36a} A. Calcaterra,^{19a} G. F. Cao,¹ S. A. Cetin,^{36b} J. F. Chang,¹ G. Chelkov,^{21,b} G. Chen,¹ H. S. Chen,¹ J. C. Chen,¹ M. L. Chen,¹ S. J. Chen,²⁶ X. Chen,¹ X. R. Chen,²³ Y. B. Chen,¹ H. P. Cheng,¹⁶ X. K. Chu,²⁸ Y. P. Chu,¹ D. Cronin-Hennessy,⁴⁰ H. L. Dai,¹ J. P. Dai,¹ D. Dedovich,²¹ Z. Y. Deng,¹ A. Denig,²⁰ I. Denysenko,²¹ M. Destefanis,^{45a,45c} W. M. Ding,³⁰ Y. Ding,²⁴ C. Dong,²⁷ J. Dong,¹ L. Y. Dong,¹ M. Y. Dong,¹ S. X. Du,⁴⁹ J. Z. Fan,³⁵ J. Fang,¹ S. S. Fang,¹ Y. Fang,¹ L. Fava,^{45b,45c} C. Q. Feng,⁴² C. D. Fu,¹ O. Fuks,^{21,b} Q. Gao,¹ Y. Gao,³⁵ C. Geng,⁴² K. Goetzen,⁹ W. X. Gong,¹ W. Gradl,²⁰ M. Greco,^{45a,45c} M. H. Gu,¹ Y. T. Gu,¹¹ Y. H. Guan,¹ A. Q. Guo,²⁷ L. B. Guo,²⁵ T. Guo,²⁵ Y. P. Guo,²⁰ Y. L. Han,¹ F. A. Harris,³⁹ K. L. He,¹ M. He,¹ Z. Y. He,²⁷ T. Held,³ Y. K. Heng,¹ Z. L. Hou,¹ C. Hu,²⁵ H. M. Hu,¹ J. F. Hu,³⁷ T. Hu,¹ G. M. Huang,⁵ G. S. Huang,⁴² H. P. Huang,⁴⁷ J. S. Huang,¹⁴ L. Huang,¹ X. T. Huang,³⁰ Y. Huang,²⁶ T. Hussain,⁴⁴ C. S. Ji,⁴² Q. Ji,¹ Q. P. Ji,²⁷ X. B. Ji,¹ X. L. Ji,¹ L. L. Jiang,¹ L. W. Jiang,⁴⁷ X. S. Jiang,¹ J. B. Jiao,³⁰ Z. Jiao,¹⁶ D. P. Jin,¹ S. Jin,¹ T. Johansson,⁴⁶ N. Kalantar-Nayestanaki,²² X. L. Kang,¹ X. S. Kang,²⁷ M. Kavatsyuk,²² B. Kloss,²⁰ B. Kopf,³ M. Kornicer,³⁹ W. Kuehn,³⁷ A. Kupsc,⁴⁶ W. Lai,¹ J. S. Lange,³⁷ M. Lara,¹⁸ P. Larin,¹³ M. Leyhe,³ C. H. Li,¹ Cheng Li,⁴² Cui Li,⁴² D. Li,¹⁷ D. M. Li,⁴⁹ F. Li,¹ G. Li,¹ H. B. Li,¹ J. C. Li,¹ K. Li,³⁰ K. Li,¹² Lei Li,¹ P. R. Li,³⁸ Q. J. Li,¹ T. Li,³⁰ W. D. Li,¹ W. G. Li,¹ X. L. Li,³⁰ X. N. Li,¹ X. Q. Li,²⁷ Z. B. Li,³⁴ H. Liang,⁴² Y. F. Liang,³² Y. T. Liang,³⁷ D. X. Lin,¹³ B. J. Liu,¹ C. L. Liu,⁴ C. X. Liu,¹ F. H. Liu,³¹ Fang Liu,¹ Feng Liu,⁵ H. B. Liu,¹¹ H. H. Liu,¹⁵ H. M. Liu,¹ J. Liu,¹ J. P. Liu,⁴⁷ K. Liu,³⁵ K. Y. Liu,²⁴ P. L. Liu,³⁰ Q. Liu,³⁸ S. B. Liu,⁴² X. Liu,²³ Y. B. Liu,²⁷ Z. A. Liu,¹ Zhiqiang Liu,¹ Zhiqing Liu,²⁰ H. Loehner,²² X. C. Lou,^{1,c} G. R. Lu,¹⁴ H. J. Lu,¹⁶ H. L. Lu,¹ J. G. Lu,¹ X. R. Lu,³⁸ Y. Lu,¹ Y. P. Lu,¹ C. L. Luo,²⁵ M. X. Luo,⁴⁸ T. Luo,³⁹ X. L. Luo,¹ M. Lv,¹ F. C. Ma,²⁴ H. L. Ma,¹ Q. M. Ma,¹ S. Ma,¹ T. Ma,¹ X. Y. Ma,¹ F. E. Maas,¹³ M. Maggiora,^{45a,45c} Q. A. Malik,⁴⁴ Y. J. Mao,²⁸ Z. P. Mao,¹ J. G. Messchendorp,²² J. Min,¹ T. J. Min,¹ R. E. Mitchell,¹⁸ X. H. Mo,¹ Y. J. Mo,⁵ H. Moeini,²² C. Morales Morales,¹³ K. Moriya,¹⁸ N. Yu. Muchnoi,^{8,a} H. Muramatsu,⁴⁰ Y. Nefedov,²¹ I. B. Nikolaev,^{8,a} Z. Ning,¹ S. Nisar,⁷ X. Y. Niu,¹ S. L. Olsen,²⁹ Q. Ouyang,¹ S. Pacetti,^{19b} M. Pelizaeus,³ H. P. Peng,⁴² K. Peters,⁹ J. L. Ping,²⁵ R. G. Ping,¹ R. Poling,⁴⁰ N. Q.,⁴⁷ M. Qi,²⁶ S. Qian,¹ C. F. Qiao,³⁸ L. Q. Qin,³⁰ X. S. Qin,¹ Y. Qin,²⁸ Z. H. Qin,¹ J. F. Qiu,¹ K. H. Rashid,⁴⁴ C. F. Redmer,²⁰ M. Ripka,²⁰ G. Rong,¹ X. D. Ruan,¹¹ A. Sarantsev,^{21,d} K. Schoenning,⁴⁶ S. Schumann,²⁰ W. Shan,²⁸ M. Shao,⁴² C. P. Shen,² X. Y. Shen,¹ H. Y. Sheng,¹ M. R. Shepherd,¹⁸ W. M. Song,¹ X. Y. Song,¹ S. Spataro,^{45a,45c} B. Spruck,³⁷ G. X. Sun,¹ J. F. Sun,¹⁴ S. S. Sun,¹ Y. J. Sun,⁴² Y. Z. Sun,¹ Z. J. Sun,¹ Z. T. Sun,⁴² C. J. Tang,⁵² X. Tang,¹ I. Tapan,^{36c} E. H. Thorndike,⁴¹ D. Toth,⁴⁰ M. Ullrich,³⁷ I. Uman,^{36b} G. S. Varner,³⁹ B. Wang,²⁷ D. Wang,²⁸ D. Y. Wang,²⁸ K. Wang,¹ L. L. Wang,¹ L. S. Wang,¹ M. Wang,³⁰ P. Wang,¹ P. L. Wang,¹ Q. J. Wang,¹ S. G. Wang,²⁸ W. Wang,¹ X. F. Wang,³⁵ Y. D. Wang,^{19a} Y. F. Wang,¹ Y. Q. Wang,²⁰ Z. Wang,¹ Z. G. Wang,¹ Z. H. Wang,⁴² Z. Y. Wang,¹ D. H. Wei,¹⁰ J. B. Wei,²⁸ P. Weidenkaff,²⁰ S. P. Wen,¹ M. Werner,³⁷ U. Wiedner,³ M. Wolke,⁴⁶ L. H. Wu,¹ N. Wu,¹ Z. Wu,¹ L. G. Xia,³⁵ Y. Xia,¹⁷ D. Xiao,¹ Z. J. Xiao,²⁵ Y. G. Xie,¹ Q. L. Xiu,¹ G. F. Xu,¹ L. Xu,¹ Q. J. Xu,¹² Q. N. Xu,³⁸ X. P. Xu,³³ Z. Xue,¹ L. Yan,⁴² W. B. Yan,⁴² W. C. Yan,⁴² Y. H. Yan,¹⁷ H. X. Yang,¹ L. Yang,⁴⁷ Y. Yang,⁵ Y. X. Yang,¹⁰ H. Ye,¹ M. Ye,¹ M. H. Ye,⁶ B. X. Yu,¹ C. X. Yu,²⁷ H. W. Yu,²⁸ J. S. Yu,²³ S. P. Yu,³⁰ C. Z. Yuan,¹ W. L. Yuan,²⁶ Y. Yuan,¹ A. Yuncu,^{36b} A. A. Zafar,⁴⁴ A. Zallo,^{19a} S. L. Zang,²⁶ Y. Zeng,¹⁷ B. X. Zhang,¹ B. Y. Zhang,¹ C. Zhang,²⁶ C. B. Zhang,¹⁷ C. C. Zhang,¹ D. H. Zhang,¹ H. H. Zhang,³⁴ H. Y. Zhang,¹ J. J. Zhang,¹ J. Q. Zhang,¹ J. W. Zhang,¹ J. Y. Zhang,¹ J. Z. Zhang,¹ S. H. Zhang,¹ X. J. Zhang,¹ X. Y. Zhang,³⁰ Y. Zhang,¹ Y. H. Zhang,¹ Z. H. Zhang,⁵ Z. P. Zhang,⁴² Z. Y. Zhang,⁴⁷ G. Zhao,¹ J. W. Zhao,¹ Lei Zhao,⁴² Ling Zhao,¹ M. G. Zhao,²⁷ Q. Zhao,¹ Q. W. Zhao,¹ S. J. Zhao,⁴⁹ T. C. Zhao,¹ X. H. Zhao,²⁶ Y. B. Zhao,¹ Z. G. Zhao,⁴² A. Zhemchugov,^{21,b} B. Zheng,⁴³ J. P. Zheng,¹ Y. H. Zheng,³⁸ B. Zhong,²⁵ L. Zhou,¹ Li Zhou,²⁷ X. Zhou,⁴⁷ X. K. Zhou,³⁸ X. R. Zhou,⁴² X. Y. Zhou,¹ K. Zhu,¹ K. J. Zhu,¹ X. L. Zhu,³⁵ Y. C. Zhu,⁴² Y. S. Zhu,¹ Z. A. Zhu,¹ J. Zhuang,¹ B. S. Zou,¹ and J. H. Zou¹

(BESIII Collaboration)

¹*Institute of High Energy Physics, Beijing 100049, People's Republic of China*²*Beihang University, Beijing 100191, People's Republic of China*³*Bochum Ruhr-University, D-44780 Bochum, Germany*⁴*Carnegie Mellon University, Pittsburgh, Pennsylvania 15213, USA*⁵*Central China Normal University, Wuhan 430079, People's Republic of China*⁶*China Center of Advanced Science and Technology, Beijing 100190, People's Republic of China*⁷*COMSATS Institute of Information Technology, Lahore, Defence Road, Off Raiwind Road, 54000 Lahore, Pakistan*⁸*G. I. Budker Institute of Nuclear Physics SB RAS (BINP), Novosibirsk 630090, Russia*⁹*GSF Helmholtzcentre for Heavy Ion Research GmbH, D-64291 Darmstadt, Germany*¹⁰*Guangxi Normal University, Guilin 541004, People's Republic of China*

- ¹¹Guangxi University, Nanning 530004, People's Republic of China
¹²Hangzhou Normal University, Hangzhou 310036, People's Republic of China
¹³Helmholtz Institute Mainz, Johann-Joachim-Becher-Weg 45, D-55099 Mainz, Germany
¹⁴Henan Normal University, Xinxiang 453007, People's Republic of China
¹⁵Henan University of Science and Technology, Luoyang 471003, People's Republic of China
¹⁶Huangshan College, Huangshan 245000, People's Republic of China
¹⁷Hunan University, Changsha 410082, People's Republic of China
¹⁸Indiana University, Bloomington, Indiana 47405, USA
^{19a}INFN Laboratori Nazionali di Frascati, I-00044 Frascati, Italy
^{19b}INFN and University of Perugia, I-06100 Perugia, Italy
²⁰Johannes Gutenberg University of Mainz, Johann-Joachim-Becher-Weg 45, D-55099 Mainz, Germany
²¹Joint Institute for Nuclear Research, 141980 Dubna, Moscow Region, Russia
²²KVI, University of Groningen, NL-9747 AA Groningen, The Netherlands
²³Lanzhou University, Lanzhou 730000, People's Republic of China
²⁴Liaoning University, Shenyang 110036, People's Republic of China
²⁵Nanjing Normal University, Nanjing 210023, People's Republic of China
²⁶Nanjing University, Nanjing 210093, People's Republic of China
²⁷Nankai University, Tianjin 300071, People's Republic of China
²⁸Peking University, Beijing 100871, People's Republic of China
²⁹Seoul National University, Seoul 151-747, Korea
³⁰Shandong University, Jinan 250100, People's Republic of China
³¹Shanxi University, Taiyuan 030006, People's Republic of China
³²Sichuan University, Chengdu 610064, People's Republic of China
³³Soochow University, Suzhou 215006, People's Republic of China
³⁴Sun Yat-Sen University, Guangzhou 510275, People's Republic of China
³⁵Tsinghua University, Beijing 100084, People's Republic of China
^{36a}Ankara University, Dogol Caddesi, 06100 Tandogan, Ankara, Turkey
^{36b}Dogus University, 34722 Istanbul, Turkey
^{36c}Uludag University, 16059 Bursa, Turkey
³⁷Universitaet Giessen, D-35392 Giessen, Germany
³⁸University of Chinese Academy of Sciences, Beijing 100049, People's Republic of China
³⁹University of Hawaii, Honolulu, Hawaii 96822, USA
⁴⁰University of Minnesota, Minneapolis, Minnesota 55455, USA
⁴¹University of Rochester, Rochester, New York 14627, USA
⁴²University of Science and Technology of China, Hefei 230026, People's Republic of China
⁴³University of South China, Hengyang 421001, People's Republic of China
⁴⁴University of the Punjab, Lahore-54590, Pakistan
^{45a}University of Turin, I-10125 Turin, Italy
^{45b}University of Eastern Piedmont, I-15121 Alessandria, Italy
^{45c}INFN, I-10125 Turin, Italy
⁴⁶Uppsala University, Box 516, SE-75120 Uppsala, Sweden
⁴⁷Wuhan University, Wuhan 430072, People's Republic of China
⁴⁸Zhejiang University, Hangzhou 310027, People's Republic of China
⁴⁹Zhengzhou University, Zhengzhou 450001, People's Republic of China
(Received 10 February 2014; published 11 April 2014)

Using $(106.41 \pm 0.86) \times 10^6 \psi(3686)$ events collected with the BESIII detector at BEPCII, we study for the first time the decay $\chi_{cJ} \rightarrow \eta' K^+ K^-$ ($J = 1, 2$), where $\eta' \rightarrow \gamma \rho^0$ and $\eta' \rightarrow \eta \pi^+ \pi^-$. A partial wave analysis in the covariant tensor amplitude formalism is performed for the decay $\chi_{c1} \rightarrow \eta' K^+ K^-$. Intermediate processes $\chi_{c1} \rightarrow \eta' f_0(980)$, $\chi_{c1} \rightarrow \eta' f_0(1710)$, $\chi_{c1} \rightarrow \eta' f_2'(1525)$ and $\chi_{c1} \rightarrow K_0^*(1430)^\pm K^\mp$ ($K_0^*(1430)^\pm \rightarrow \eta' K^\pm$) are observed with statistical significances larger than 5σ , and their branching fractions are measured.

DOI: 10.1103/PhysRevD.89.074030

PACS numbers: 13.25.Gv, 14.40.Be, 14.40.Df

^aAlso at the Novosibirsk State University, Novosibirsk, 630090, Russia.^bAlso at the Moscow Institute of Physics and Technology, Moscow 141700, Russia.^cAlso at University of Texas at Dallas, Richardson, Texas 75083, USA.^dAlso at the PNPI, Gatchina 188300, Russia.

I. INTRODUCTION

Exclusive heavy quarkonium decays provide an important laboratory for investigating perturbative quantum chromodynamics (pQCD). Compared to J/ψ and $\psi(3686)$ decays, relatively little is known concerning χ_{cJ} decays [1]. More experimental data on exclusive decays of P -wave charmonia are important for a better understanding of the decay dynamics of the χ_{cJ} ($J = 0, 1, 2$) states, as well as testing QCD based calculations. Although these χ_{cJ} states are not directly produced in e^+e^- collisions, they are produced copiously in $\psi(3686)$ $E1$ transitions, with branching fractions around 9% [1] each. The large $\psi(3686)$ data sample taken with the Beijing Spectrometer (BESIII) located at the Beijing Electron-Positron Collider (BEPCII) provides an opportunity for a detailed study of χ_{cJ} decays.

QCD theory allows the existence of glueballs, and glueballs are expected to mix strongly with nearby conventional $q\bar{q}$ states [2]. For hadronic decays of the χ_{c1} , two-gluon annihilation in pQCD is suppressed by the Landau-Yang theorem [3] in the on-shell limit. As a result, the annihilation is expected to be dominated by the pQCD hair-pin diagram. The decay $\chi_{c1} \rightarrow PS$, where P and S denote a pseudoscalar and a scalar meson, respectively, is expected to be sensitive to the quark contents of the final-state scalar meson. And by tagging the quark contents of the recoiling pseudoscalar meson, the process can be used in testing the glueball- $q\bar{q}$ mixing relations among the scalar mesons S , i.e. $f_0(1370)$, $f_0(1500)$, $f_0(1710)$. A detailed calculation can be found in Ref. [4].

The $K_0^*(1430)$ state is perhaps the least controversial of the light scalar isobar mesons [1]. Its properties are still interesting since it is highly related to the line shape of the controversial κ meson ($K\pi$ S -wave scattering at mass threshold) in various studies. Until now, $K_0^*(1430)$ has been observed in $K_0^*(1430) \rightarrow K\pi$ only, but it is also expected to couple to $\eta'K$ [5,6]. The opening of the $\eta'K$ channel will affect its line shape. $\chi_{c1} \rightarrow \eta'K^+K^-$ is a promising channel to search for $K_0^*(1430)$ and study its properties. The decays $\chi_{c0,2} \rightarrow K_0^*(1430)K$ are forbidden by spin-parity conservation.

In this paper, we study the decay $\chi_{cJ} \rightarrow \eta'K^+K^-$ with $\eta' \rightarrow \gamma\rho^0$ (mode I) and $\eta' \rightarrow \eta\pi^+\pi^-$, $\eta \rightarrow \gamma\gamma$ (mode II). Only results for χ_{c1} and χ_{c2} are given, because $\chi_{c0} \rightarrow \eta'K^+K^-$ is forbidden by spin-parity conservation. A partial wave analysis (PWA) in the covariant tensor amplitude formalism is performed for the process χ_{c1} , and results on intermediate processes involved are given. For $\chi_{c2} \rightarrow \eta'K^+K^-$, due to low statistics, a simple PWA is performed, and the result is used to estimate the event selection efficiency. The data sample used in this analysis consists of 156.4 pb^{-1} of data taken at $\sqrt{s} = 3.686 \text{ GeV}/c^2$ corresponding to $(106.41 \pm 0.86) \times 10^6 \psi(3686)$ events [7].

II. DETECTOR AND MONTE CARLO SIMULATION

BESIII [8] is a general purpose detector at the BEPCII accelerator for studies of hadron spectroscopy as well as τ -charm physics [9]. The design peak luminosity of the double-ring e^+e^- collider, BEPCII, is $10^{33} \text{ cm}^{-2}\text{s}^{-1}$ at center-of-mass energy of 3.78 GeV. The BESIII detector with a geometrical acceptance of 93% of 4π , consists of the following main components: (1) A small-cell, helium-based main drift chamber (MDC) with 43 layers, which measures tracks of charged particles and provides a measurement of the specific energy loss dE/dx . The average single wire resolution is $135 \mu\text{m}$, and the momentum resolution for 1 GeV/ c charged particles in a 1 T magnetic field is 0.5%. (2) An electromagnetic calorimeter (EMC) consisting of 6240 CsI(Tl) crystals arranged in a cylindrical shape (barrel) plus two end caps. For 1.0 GeV/ c photons, the energy resolution is 2.5% (5%) in the barrel (end caps), and the position resolution is 6 mm (9 mm) in the barrel (end caps). (3) A time-of-flight system (TOF) for particle identification (PID) composed of a barrel part constructed of two layers with 88 pieces of 5 cm thick, 2.4 m long plastic scintillators in each layer, and two end caps with 48 fan-shaped, 5 cm thick, plastic scintillators in each end cap. The time resolution is 80 ps (110 ps) in the barrel (end caps), corresponding to a K/π separation by more than 2σ for momenta below about 1 GeV/ c . (4) A muon chamber system consists of 1000 m^2 of resistive plate chambers arranged in 9 layers in the barrel and 8 layers in the end caps and incorporated in the return iron yoke of the superconducting magnet. The position resolution is about 2 cm.

The optimization of the event selection and the estimation of backgrounds are performed through Monte Carlo (MC) simulation. The GEANT 4-based simulation software BOOST [10] includes the geometric and material description of the BESIII detectors and the detector response and digitization models, as well as the tracking of the detector running conditions and performance. The production of the $\psi(3686)$ resonance is simulated by the MC event generator KKMC [11], while the decays are generated by EVTGEN [12] for known decay modes with branching fractions being set to world average values [1], and by LUNDCHARM [13] for the remaining unknown decays.

III. EVENT SELECTION

The final states of the sequential decay $\psi(3686) \rightarrow \gamma\chi_{cJ}$, $\chi_{cJ} \rightarrow \eta'K^+K^-$ have the topologies $\gamma\gamma K^+K^-\pi^+\pi^-$ or $\gamma\gamma\gamma K^+K^-\pi^+\pi^-$ for η' decay modes I or II, respectively. Event candidates are required to have four charged tracks and at least two (three) good photons for mode I (II).

Charged tracks in the polar angle range $|\cos\theta| < 0.93$ are reconstructed from MDC hits. The closest point to the beam line of each selected track should be within $\pm 10 \text{ cm}$

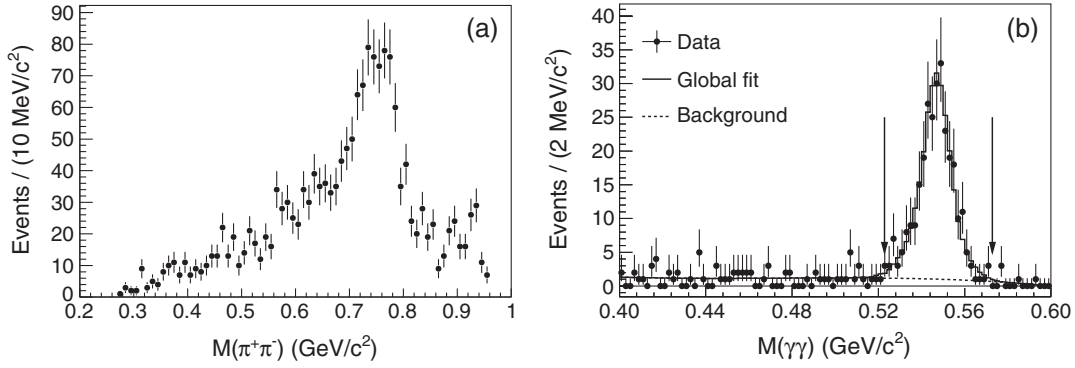


FIG. 1. The invariant mass distributions of (a) $\pi^+\pi^-$ in mode I, and (b) $\gamma\gamma$ in mode II. The arrows show the η signal region.

of the interaction point in the beam direction, and within 1 cm in the plane perpendicular to the beam. The candidate events are required to have four well-reconstructed charged tracks with net charge zero. TOF and dE/dx information is combined to form PID confidence levels for the π , K and p hypotheses. Kaons are identified by requiring the PID probability ($Prob$) to be $Prob(K) > Prob(\pi)$ and $Prob(K) > Prob(p)$. Two identified kaons with opposite charge are required. The other two charged tracks are assumed to be pions.

Photon candidates are reconstructed by clustering signals in EMC crystals. The photon candidates in the barrel ($|\cos\theta| < 0.80$) of the EMC are required to have at least 25 MeV total energy deposition, or in the end cap ($0.86 < |\cos\theta| < 0.92$) at least 50 MeV total energy deposition, where θ is the polar angle of the shower. The photon candidates are further required to be isolated from all charged tracks by an angle $> 5^\circ$ to suppress showers from charged particles. Timing information from the EMC is used to suppress electronic noise and energy deposition unrelated to the event.

A four-constraint (4C) energy-momentum conserving kinematic fit is applied to candidate events under the $\gamma\gamma(\gamma)K^+K^-\pi^+\pi^-$ hypothesis. For events with more than two (three) photon candidates, all of the possible two (three) photon combinations are fitted, and the candidate combination with the minimum χ^2_{4C} is selected, and it is required that $\chi^2_{4C} < 40(50)$.

In the η' decay mode I, the photon with the smaller $|M(\gamma\pi^+\pi^-) - M(\eta')|$ is assigned as the photon from η' decay, and the other one is tagged as the photon from the radiative decay of $\psi(3686)$. The mass requirement $|M(\gamma\gamma) - M(\pi^0)| > 15 \text{ MeV}/c^2$ is applied to remove backgrounds with π^0 in the final state. $|M(\pi^+\pi^-)_{\text{rec}} - M(J/\psi)| > 8 \text{ MeV}/c^2$ and $|M(\gamma\gamma)_{\text{rec}} - M(J/\psi)| > 22 \text{ MeV}/c^2$ are further used to suppress backgrounds from $\psi(3686) \rightarrow \pi^+\pi^-J/\psi$ with $J/\psi \rightarrow (\gamma/\pi^0/\gamma\pi^0)K^+K^-$, as well as from $\psi(3686) \rightarrow \gamma\chi_{cJ}$ or $\psi(3686) \rightarrow (\eta/\pi^0)J/\psi$ with $J/\psi \rightarrow K^+K^-\pi^+\pi^-$, where $M(\pi^+\pi^-)_{\text{rec}}$ and $M(\gamma\gamma)_{\text{rec}}$ are the recoil masses from the $\pi^+\pi^-$ and $\gamma\gamma$ systems, respectively. Figure 1(a) shows the invariant mass

distribution of $\pi^+\pi^-$, and a clear ρ^0 signal is observed. For the η' decay mode II, candidate events are rejected if any pair of photons has $|M(\gamma\gamma) - M(\pi^0)| < 20 \text{ MeV}/c^2$, in order to suppress backgrounds with π^0 in the final state. The η candidate is selected as the photon pair whose invariant mass is closest to the η mass [1]. The $M(\gamma\gamma)$ distribution, shown in Fig. 1(b), is fitted with the MC simulated η signal shape plus a third order polynomial background function. $|M(\gamma\gamma) - M(\eta)| < 25 \text{ MeV}/c^2$ is required to select the η signal.

After the above event selection, the invariant mass distributions of $\gamma\pi^+\pi^-$ and of $\gamma\gamma\pi^+\pi^-$ in the two η' decay modes are shown in Fig. 2. The η' signals are seen clearly, and the distributions are fitted with the MC simulated η' signal shape plus a third order polynomial function for the background. $|M(\gamma\pi^+\pi^-) - M(\eta')| < 15 \text{ MeV}/c^2$ and $|M(\eta\pi^+\pi^-) - M(\eta')| < 25 \text{ MeV}/c^2$ are used to select the η' signal in the two decay modes, respectively.

IV. BACKGROUND STUDIES

The scatter plots of the invariant mass of $\gamma(\gamma)\pi^+\pi^-K^+K^-$ versus that of $\gamma(\gamma)\pi^+\pi^-$ are shown in Fig. 3(a) (mode I) and Fig. 4(a) (mode II), respectively. Two clusters of events in the $\chi_{c1,2}$ and η' signal regions, which arise from the signal processes of $\psi(3686) \rightarrow \gamma\chi_{c1,2}$, $\chi_{c1,2} \rightarrow \eta'K^+K^-$, are clearly visible. Clear χ_{cJ} bands are also observed outside the η' signal region.

Inclusive and exclusive MC studies are carried out to investigate potential backgrounds. The dominant backgrounds are found to be $\psi(3686) \rightarrow \gamma\chi_{cJ}$, $\chi_{cJ} \rightarrow K^+K^-\pi^+\pi^-$, $(\pi^0/\gamma_{\text{FSR}})K^+K^-\pi^+\pi^-$ for mode I or $\chi_{cJ} \rightarrow \eta\pi^+\pi^-K^+K^-$ (no η' formed) for mode II. Also for mode II, there are small contaminations from the decays $\psi(3686) \rightarrow \gamma\chi_{cJ}$, $\chi_{cJ} \rightarrow \pi^0\pi^+\pi^-K^+K^-$ and $\chi_{cJ} \rightarrow \gamma J/\psi$ with $J/\psi \rightarrow (\gamma/\pi^0)\pi^+\pi^-K^+K^-$. All these backgrounds have exactly the same topology, or have one less (more) photon than the signal process, but no η' intermediate state. They will produce peaking background in the $\gamma(\gamma)\pi^+\pi^-K^+K^-$ invariant mass distribution within the χ_{cJ} region. The $\gamma(\gamma)\pi^+\pi^-K^+K^-$ invariant mass

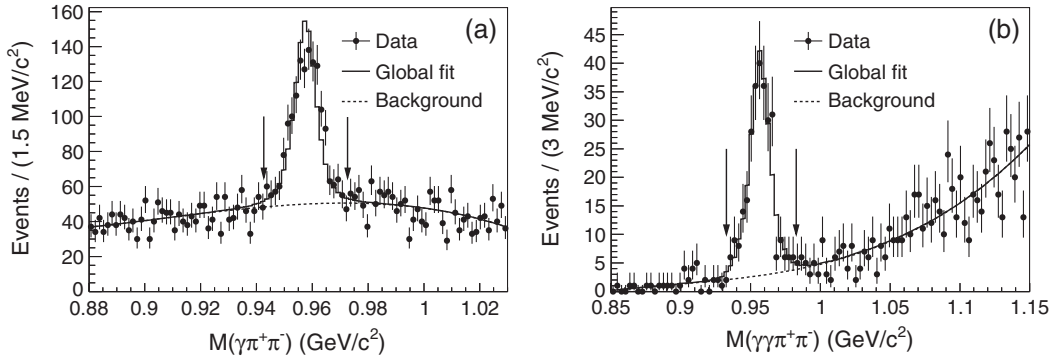


FIG. 2. The invariant mass distributions of (a) $\gamma\pi^+\pi^-$ in the decay mode I, and (b) $\gamma\gamma\pi^+\pi^-$ in the decay mode II. The arrows show the η' signal region.

distributions of events with $\gamma(\gamma)\pi^+\pi^-$ mass outside the η' signal region ($|M(\gamma\pi^+\pi^-) - M(\eta')| > 15 \text{ MeV}/c^2$, $|M(\gamma\gamma\pi^+\pi^-) - M(\eta')| > 25 \text{ MeV}/c^2$) for the two η' decay modes are shown in Fig. 3(b) and Fig. 4(b), respectively. The distributions are fitted with the sum of three Gaussian functions together with a third order polynomial function, which represent the peaking backgrounds and nonpeaking background, respectively. The peaking background shape obtained here will be used in the following fit as the peaking background shape within the η' signal range.

V. SIGNAL DETERMINATION

To determine the signal yields, a simultaneous unbinned fit is performed on the $\gamma(\gamma)K^+K^-\pi^+\pi^-$ invariant mass distributions for candidate events within the η' signal and sideband regions, where the η' sideband regions are defined as $25 \text{ MeV}/c^2 < |M(\gamma\pi^+\pi^-) - M(\eta')| < 40 \text{ MeV}/c^2$ and $35 \text{ MeV}/c^2 < M(\gamma\gamma\pi^+\pi^-) - M(\eta') < 85 \text{ MeV}/c^2$ for the two η' decay modes, respectively. The following formulas are used to fit the distributions in the signals and sideband regions, respectively

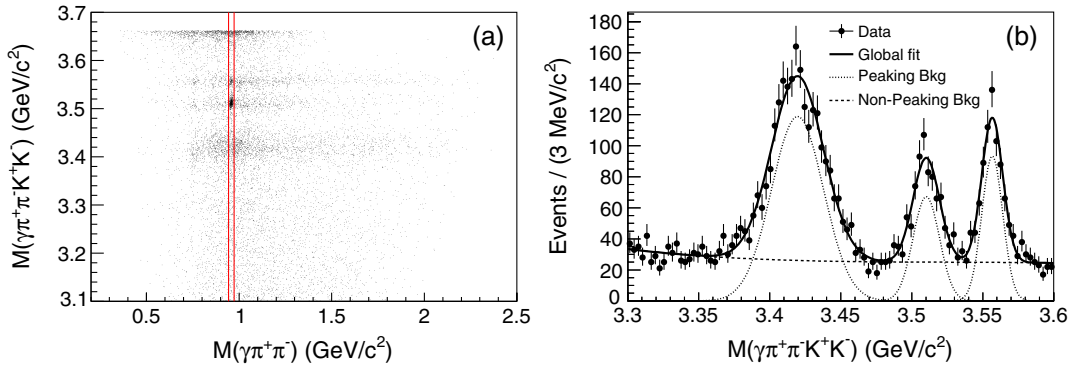


FIG. 3 (color online). (a) The scatter plot of $M(\gamma\pi^+\pi^-K^+K^-)$ versus $M(\gamma\pi^+\pi^-)$. The two vertical lines show the η' signal region. (b) The $\gamma\pi^+\pi^-K^+K^-$ invariant mass of events with $M(\gamma\pi^+\pi^-)$ outside the η' range in the η' decay mode I.

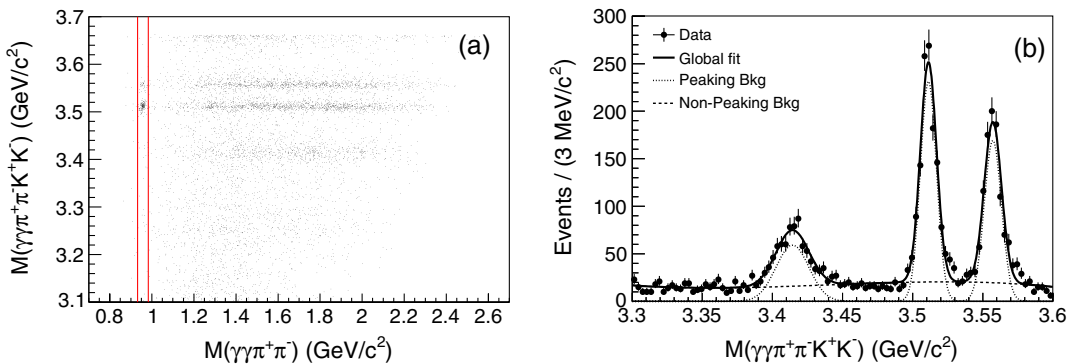


FIG. 4 (color online). (a) The scatter plot of $M(\gamma\gamma\pi^+\pi^-K^+K^-)$ versus $M(\gamma\pi^+\pi^-)$ distribution. The two vertical lines show the η' signal region. (b) The $\gamma\gamma\pi^+\pi^-K^+K^-$ invariant mass of events with $M(\gamma\pi^+\pi^-)$ outside the η' range in the η' decay mode II.

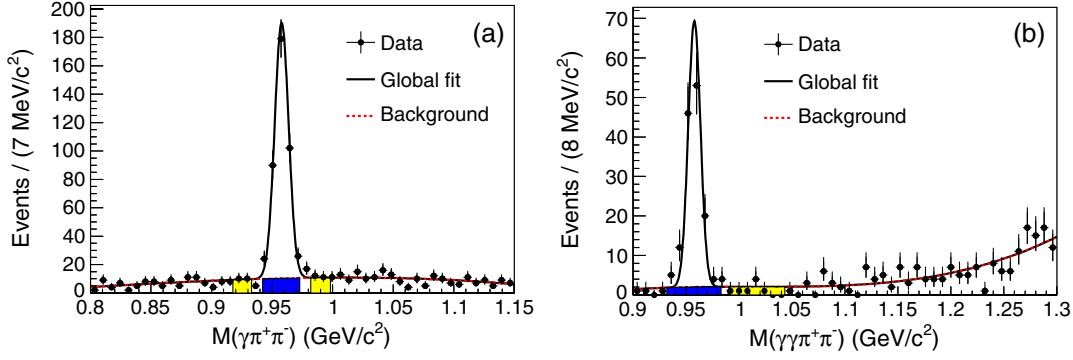


FIG. 5 (color online). The $\gamma(\gamma)\pi^+\pi^-$ mass distribution within the χ_{c1} region for (a) η' decay mode I and (b) η' decay mode II. The band under the peak shows the η' signal region, and the other bands show η' sideband.

$$f_{\text{sg}}(m) = \sum_{cJ=1}^{cJ=2} N_{cJ}^{\text{sig}} \times F_{cJ}^{\text{sig}}(m) \otimes G(m, m_i, \sigma_i) + \sum_{i=0}^{i=2} N_i^{\text{bkg}} \times F_i^{\text{bkg}}(m) + N_{\text{signal}}^{\text{BG}} \times F^{\text{BG}}(m), \quad (1)$$

$$f_{\text{sb}}(m) = \sum_{i=0}^{i=2} \alpha_i \times N_i^{\text{bkg}} \times F_i^{\text{bkg}}(m) + N_{\text{sideband}}^{\text{BG}} \times F^{\text{BG}}(m), \quad (2)$$

where $F_{cJ}^{\text{sig}}(m)$ represents the χ_{cJ} signal line shape, which is described by the MC simulated shape. $G(m, m_i, \sigma_i)$ is a Gaussian function parametrizing the instrumental resolution difference (σ_i) and mass offset (m_i) between data and MC simulation, with parameters free in the fit. Since $\chi_{c0} \rightarrow \eta' K^+ K^-$ is forbidden by spin-parity conservation, only the $\chi_{c1,2}$ signals are considered in the fit. $F_i^{\text{bkg}}(m)$ is a Gaussian function for peaking backgrounds. MC studies show that the peaking background shapes do not depend on the $\gamma(\gamma)\pi^+\pi^-$ invariant mass. In the fit, the parameters of $F_i^{\text{bkg}}(m)$ are identical for η' signal and sideband regions, and are fixed to the fitting results from the candidate events with $\gamma(\gamma)\pi^+\pi^-$ invariant mass out of the η' signal region [Fig. 3(b) and Fig. 4(b)]. $F^{\text{BG}}(m)$ represents the non-peaking background which is parametrized as a third order polynomial function. N_{cJ}^{sig} , N_i^{bkg} , $N_{\text{signal}}^{\text{BG}}$ and $N_{\text{sideband}}^{\text{BG}}$ are the numbers of χ_{cJ} signal events, peaking backgrounds in η' signal region, and nonpeaking background in η' signal or sideband region, respectively, to be determined in the fit. α_i is the ratio of the number of peaking background events in the η' sideband region to that in the η' signal region. The magnitudes of α_i are fixed in the fit and the values are obtained by fitting the $\gamma(\gamma)\pi^+\pi^-$ invariant mass distributions. The detailed procedure to obtain the α_i values is described in the following.

Figures 5(a) and 5(b) show the $\gamma(\gamma)\pi^+\pi^-$ invariant mass distribution for events with $\gamma(\gamma)\pi^+\pi^- K^+ K^-$ mass within the χ_{c1} signal region for the two η' decay modes, respectively. The distributions within χ_{c0} and χ_{c2}

signal region are similar. The χ_{cJ} ($J = 0, 1, 2$) signal regions are defined as $|M(\gamma\pi^+\pi^- K^+ K^-) - M(\chi_{c0})| < 30 \text{ MeV}/c^2$, $|M(\gamma\pi^+\pi^- K^+ K^-) - M(\chi_{c1})| < 15 \text{ MeV}/c^2$, and $|M(\gamma\pi^+\pi^- K^+ K^-) - M(\chi_{c2})| < 16 \text{ MeV}/c^2$ for η' decay mode I, and $|M(\gamma\gamma\pi^+\pi^- K^+ K^-) - M(\chi_{c0})| < 36 \text{ MeV}/c^2$, $|M(\gamma\gamma\pi^+\pi^- K^+ K^-) - M(\chi_{c1})| < 18 \text{ MeV}/c^2$, and $|M(\gamma\gamma\pi^+\pi^- K^+ K^-) - M(\chi_{c2})| < 18 \text{ MeV}/c^2$ for η' decay mode II. The distributions are fitted with a Gaussian function which represents the η' signal together with a polynomial function which represents non- η' background. α_i is the ratio of integrated polynomial background function in the η' sideband region to that in the η' signal region. Here the background includes both χ_{cJ} peaking background and nonpeaking background. Studies from MC simulation and real data show that the χ_{cJ} peaking background and nonpeaking background have the same α_i , and the extracted α_i is used in the previous simultaneous fit.

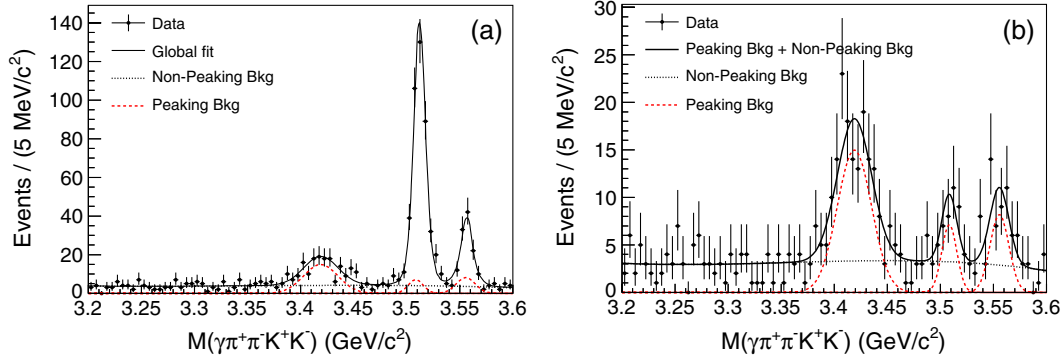
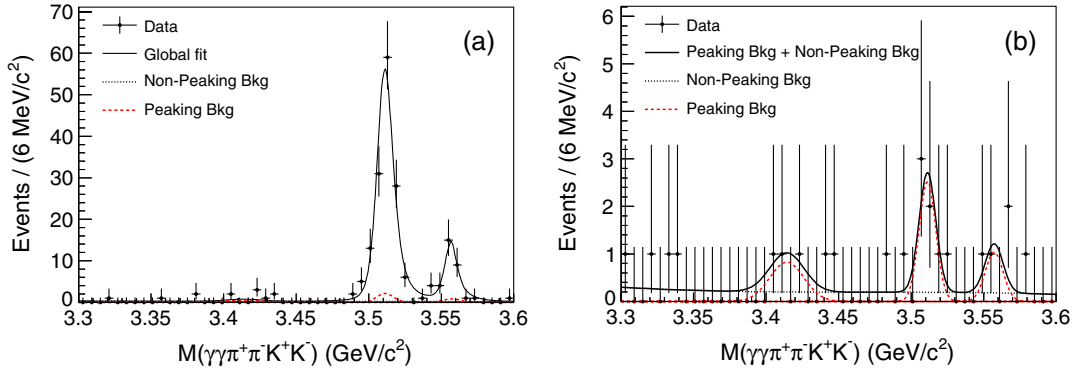
The $\gamma(\gamma)\pi^+\pi^- K^+ K^-$ invariant mass distributions of candidate events in η' signal and sideband regions for the two η' decay modes are shown in Figs. 6 and 7, respectively. The simultaneous unbinned fits are carried out to determine the signal yields, and the results are summarized in Table I.

VI. BRANCHING FRACTION

The branching fractions of $\chi_{cJ} \rightarrow \eta' K^+ K^-$ in the two η' decay modes are calculated according to

$$\mathcal{B}_1(\chi_{cJ} \rightarrow \eta' K^+ K^-) = \frac{N_{cJ}^{\text{sig}}}{N_{\psi(3686)} \times \mathcal{B}(\psi(3686) \rightarrow \gamma\chi_{cJ}) \times \mathcal{B}(\eta' \rightarrow \gamma\rho^0) \times e_{cJ}^1} \quad (3)$$

$$\mathcal{B}_2(\chi_{cJ} \rightarrow \eta' K^+ K^-) = \frac{N_{cJ}^{\text{sig}}}{N_{\psi(3686)} \times \mathcal{B}(\psi(3686) \rightarrow \gamma\chi_{cJ})} \times \frac{1}{\mathcal{B}(\eta' \rightarrow \eta\pi^+\pi^-) \times \mathcal{B}(\eta \rightarrow \gamma\gamma) \times e_{cJ}^2} \quad (4)$$

FIG. 6 (color online). Invariant mass distribution of $\gamma\pi^+\pi^-K^+K^-$ for η' decay mode I in (a) η' signal region and (b) η' sideband region.FIG. 7 (color online). Invariant mass distribution of $\gamma\gamma\pi^+\pi^-K^+K^-$ for the η' decay mode II in (a) η' signal region and (b) η' sideband region. The fraction of nonpeaking background is very small so its line is invisible in the left plot.

where N_{cJ}^{sig} is the number of signal events extracted from the simultaneous unbinned fit. $N_{\psi(3686)}$ is the number of $\psi(3686)$ events. $\mathcal{B}(\psi(3686) \rightarrow \gamma\chi_{cJ})$, $\mathcal{B}(\eta' \rightarrow \gamma\rho^0)$, $\mathcal{B}(\eta' \rightarrow \eta\pi^+\pi^-)$ and $\mathcal{B}(\eta \rightarrow \gamma\gamma)$ are branching fractions from the PDG [1]. ϵ_{cJ}^1 and ϵ_{cJ}^2 are the detection efficiencies for mode I and mode II, respectively. Detailed studies in Sec. VIII show that abundant structures are observed in the K^+K^- and $\eta'K^\pm$ invariant mass spectra. To get the detection efficiencies properly, a PWA using covariant tensor amplitudes is performed on the candidate events, and the detection efficiencies are obtained from MC samples generated with the differential cross section from the PWA results. The detection efficiencies and the branching fractions (statistical uncertainty only) are also shown in Table I.

VII. ESTIMATION OF SYSTEMATIC UNCERTAINTIES

Several sources of systematic uncertainties are considered in the measurement of branching fractions. These include the differences between data and MC simulation for the tracking, PID, photon detection, kinematic fit, fitting procedure and number of $\psi(3686)$ events as well as the uncertainties in intermediate resonance decay branching fractions.

- (a) *Tracking and PID*: The uncertainties from tracking and PID efficiency of the kaon are investigated using an almost background free control sample of $J/\psi \rightarrow K_S^0 K^\pm \pi^\mp$ from $(225.2 \pm 2.8) \times 10^6 J/\psi$ decays [14]. Both kaon tracking efficiency and PID efficiency are

TABLE I. Summary for the fit results, detection efficiencies and branching fractions (statistical uncertainty only).

		N_{cJ}^{sig}	N_i^{bkg}	α_i	$\epsilon(\%)$	$\mathcal{B}(\chi_{cJ} \rightarrow \eta' K^+ K^-)(10^{-4})$
χ_{c0}	$\eta' \rightarrow \gamma\rho^0$...	121 ± 11	0.977 ± 0.002
	$\eta' \rightarrow \eta\pi^+\pi^-$...	3 ± 2	1.7 ± 0.3
χ_{c1}	$\eta' \rightarrow \gamma\rho^0$	388 ± 23	25 ± 7	0.984 ± 0.004	14.88	9.09 ± 0.54
	$\eta' \rightarrow \eta\pi^+\pi^-$	141 ± 13	5 ± 2	1.3 ± 0.3	10.14	8.33 ± 0.77
χ_{c2}	$\eta' \rightarrow \gamma\rho^0$	77 ± 13	36 ± 8	0.979 ± 0.003	15.38	1.84 ± 0.31
	$\eta' \rightarrow \eta\pi^+\pi^-$	30 ± 6	2 ± 2	1.4 ± 0.4	9.25	2.05 ± 0.41

studied as a function of transverse momentum and polar angle. The data-MC simulation differences are estimated to be 1% per track for the tracking efficiency and 2% [15] per track for the PID efficiency. Therefore, 2% uncertainty for the tracking efficiency and 4% uncertainty for the PID efficiency are taken as the systematic uncertainties for two kaons. The uncertainty for the pion tracking is investigated with high statistics, low background samples of $J/\psi \rightarrow \rho\pi$, $J/\psi \rightarrow p\bar{p}\pi^+\pi^-$ and $\psi(3686) \rightarrow \pi^+\pi^-J/\psi$ with $J/\psi \rightarrow l^+l^-$ events. The systematic uncertainty is taken to be 1% per track [16], and 2% for two pions.

- (b) *Photon detection efficiency*: The uncertainty due to photon detection and reconstruction is 1% per photon [15]. This value is determined from studies using clean control samples, such as $J/\psi \rightarrow \rho^0\pi^0$ and $e^+e^- \rightarrow \gamma\gamma$. Therefore, uncertainties of 2% and 3% are taken for photon detection efficiencies in the two η' decay modes, respectively.
- (c) *Kinematic fit*: To investigate the systematic uncertainty from the 4C kinematic fit, a clean control sample of $J/\psi \rightarrow \eta\phi$, $\eta \rightarrow \pi^+\pi^-\pi^0$, $\phi \rightarrow K^+K^-$, which has a similar final state to those of this analysis, is selected. A 4 C kinematic fit is applied to the control sample, and the corresponding efficiency is estimated from the ratio of the number of events with and without the kinematic fit. The difference of efficiency between data and MC simulation, 3.3%, is taken as the systematic uncertainty.
- (d) *Mass window requirements*: Several mass window requirements are applied in the analysis. In mode I, mass windows on $M(\gamma\gamma)_{\text{rec}}$ and $M(\pi^+\pi^-)_{\text{rec}}$ are applied to suppress backgrounds with J/ψ intermediate states, $M(\gamma\gamma)$ requirements are used to remove backgrounds with π^0 in the final state, and an $M(\gamma\pi^+\pi^-)$ requirement is used to determine the η' signal. In mode II, mass windows on $M(\gamma\gamma)$ are used to remove backgrounds with π^0 and to determine the η signal. An $M(\gamma\pi^+\pi^-)$ mass window is used for the η' signal. Different values of these mass window requirements within $3\sigma \sim 5\sigma$ (σ is the corresponding mass resolution) have been used, and the largest differences in the branching fractions are taken as systematic uncertainties.
- (e) *Fitting procedure*: As described above, the yields of the χ_{cJ} signal events are derived from the simultaneous unbinned fits to the invariant mass of $\gamma(\gamma)K^+K^-\pi^+\pi^-$ with $\gamma(\gamma)\pi^+\pi^-$ invariant mass within the η' signal and sideband regions for the two η' decay modes, respectively. To evaluate the systematic uncertainty associated with the fitting procedure, the following aspects have been studied. (1) *Shape of nonpeaking background*: The uncertainties due to the nonpeaking background parametrization are estimated by the difference when we use a second or fourth instead

of a third order background polynomial function. (2) *Shape of peaking backgrounds*: In the nominal fit, shapes of peaking backgrounds are fixed to the fitting results of events with $\gamma(\gamma)\pi^+\pi^-$ mass outside the η' signal region [Fig. 3(b), Fig. 4(b)]. Alternative shapes of peaking background obtained from different $\gamma(\gamma)\pi^+\pi^-$ regions are used to constrain the shape of peaking background in the fit, and to estimate the corresponding systematic uncertainty. (3) *Fitting range*: A series of fits with different intervals on the $\gamma(\gamma)K^+K^-\pi^+\pi^-$ invariant mass spectrum are performed. (4) *Sideband range*: The candidate events with $\gamma(\gamma)\pi^+\pi^-$ invariant mass within the η' sideband region are used to constrain the amplitude of peaking backgrounds in the fits. The corresponding systematic uncertainties are estimated with different interval of sideband ranges with width from $1\sigma_{\eta'}$ to $3\sigma_{\eta'}$ ($\sigma_{\eta'}$ is the width of the nominal sideband range). (5) *The normalization factor*: The normalization factors α_i are varied within their uncertainties listed in Table I. The systematic uncertainties of these aspects are taken as the largest differences in the branching fractions to the nominal result.

- (f) *Detection efficiency*: As mentioned previously, abundant structures are observed in both K^+K^- and ηK^\pm invariant mass spectra, respectively. A full PWA is performed to estimate the detection efficiencies of the χ_{c1} signal, and the following two aspects are considered to evaluate the detection efficiency uncertainties: (1) The statistical uncertainties of PWA fit parameters (the magnitudes and phases of partial waves), which are obtained from the PWA results; (2) the uncertainties of input mass and width of intermediate states [1]. For the χ_{c2} signal, a simple PWA is performed on the candidate events, and the detection efficiency uncertainties are estimated by the differences of PWA fitting with or without background subtraction.
- (g) *Other systematic uncertainties*: The number of $\psi(3686)$ events is determined from an inclusive analysis of $\psi(3686)$ hadronic events with an uncertainty of 0.8% [7]. The uncertainties due to the branching fractions of $\psi(3686) \rightarrow \gamma\chi_{cJ}$, $\eta' \rightarrow \gamma\rho^0$, $\eta' \rightarrow \eta\pi^+\pi^-$ and $\eta \rightarrow \gamma\gamma$ are taken from PDG [1].

A summary of all the uncertainties is shown in Table II. The total systematic uncertainty is obtained by summing all individual contributions in quadrature.

The final branching fractions of $\chi_{c1,2} \rightarrow \eta'K^+K^-$ measured from the two η' decay modes are listed in Table IX, where the first uncertainties are statistical, and second ones are systematic. The measured branching fractions from the two η' decay modes are consistent with each other within their uncertainties. The measurements from the two decay modes are, therefore, combined by considering the correlation of uncertainties between the two measurements, the mean value and the uncertainty are calculated with [17],

TABLE II. Summary of systematic uncertainties (in %) for the branching fractions $\chi_{c1,2} \rightarrow \eta' K^+ K^-$. The items with * are common uncertainties of two η' decay modes.

Source	$\eta' \rightarrow \gamma \rho^0$		$\eta' \rightarrow \eta \pi^+ \pi^-$	
	$\chi_{c1}(\%)$	$\chi_{c2}(\%)$	$\chi_{c1}(\%)$	$\chi_{c2}(\%)$
Tracking efficiency*	4.0	4.0	4.0	4.0
Particle identification*	4.0	4.0	4.0	4.0
Photon detection efficiency*	2.0	2.0	3.0	3.0
4C kinematic fit	3.3	3.3	3.3	3.3
Mass windows	0.8	12.5	2.6	3.9
Nonpeaking background shape	1.6	0.0	0.7	3.0
Peaking background shape	3.4	5.2	1.0	0.0
Fit range	2.2	2.7	0.7	3.0
Sideband range	0.2	7.6	0.7	3.0
Normalization factor	0.0	0.1	1.1	3.3
Efficiency	0.4	2.7	0.7	4.6
Number of $\psi(3686)$ events*	0.8	0.8	0.8	0.8
$\mathcal{B}(\psi(3686) \rightarrow \gamma \chi_{cJ})^*$	4.3	3.9	4.3	3.9
$\mathcal{B}(\eta' \rightarrow \gamma \rho^0 / \eta \pi^+ \pi^-)$	2.0	2.0	1.6	1.6
$\mathcal{B}(\eta \rightarrow \gamma \gamma)$	0.5	0.5
Total	9.5	18.0	9.2	12.0

$$\bar{x} \pm \sigma(\bar{x}) = \frac{\sum_j (x_j \cdot \sum_i \omega_{ij})}{\sum_i \sum_j \omega_{ij}} \pm \sqrt{\frac{1}{\sum_i \sum_j \omega_{ij}}}, \quad (5)$$

where i and j are summed over all decay modes, ω_{ij} is the element of the weight matrix $W = V_x^{-1}$, and V_x is the covariance error matrix calculated according to the statistical uncertainties listed in Table I and the systematic uncertainties listed in Table II. When combining the results of the two decay modes, the error matrix can be calculated as

$$V = \begin{pmatrix} \sigma_1^2 + \epsilon_f^2 x_1^2 & \epsilon_f^2 x_1 x_2 \\ \epsilon_f^2 x_1 x_2 & \sigma_2^2 + \epsilon_f^2 x_2^2 \end{pmatrix}, \quad (6)$$

where σ_i is the independent absolute uncertainty (the statistical uncertainty and all independent systematic uncertainties added in quadrature) in the measurement mode i , and ϵ_f is the common relative systematic uncertainties between the two measurements (All the common systematic uncertainties added in quadrature. The items in Table II with * are common uncertainties, and the other items are independent uncertainties). x_i is the measured value given by mode i . Then the combined mean value and combined uncertainty can be calculated as

$$\bar{x} = \frac{x_1 \sigma_2^2 + x_2 \sigma_1^2}{\sigma_1^2 + \sigma_2^2 + (x_1 - x_2)^2 \epsilon_f^2}. \quad (7)$$

$$\sigma^2(\bar{x}) = \frac{\sigma_1^2 \sigma_2^2 + (x_1^2 \sigma_2^2 + x_2^2 \sigma_1^2) \epsilon_f^2}{\sigma_1^2 + \sigma_2^2 + (x_1 - x_2)^2 \epsilon_f^2}. \quad (8)$$

The calculated results are shown in Table IX.

VIII. PARTIAL WAVE ANALYSIS OF $\chi_{c1} \rightarrow \eta' K^+ K^-$

As shown in Fig. 8, there are abundant structures observed in the $K^+ K^-$ and $\eta' K^\pm$ invariant mass distributions. In the $K^+ K^-$ invariant mass spectrum, an $f_0(980)$ is observed at $K^+ K^-$ threshold. There are also structures observed around $1.5 \text{ GeV}/c^2$ and $1.7 \text{ GeV}/c^2$. In the $\eta' K^\pm$ invariant mass spectrum, a structure is observed at threshold, which might be a $K_0^{*\pm}(1430)$ or other excited kaon with different J^P at around $1.4 \text{ GeV}/c^2$. To study the subprocesses with different intermediate states and to evaluate the detection efficiencies of the decay $\chi_{cJ} \rightarrow \eta' K^+ K^-$ properly, a PWA is performed on χ_{cJ} signal candidates with the combined data of the two η' decay modes.

A. Decay amplitude and likelihood construction

In the PWA, the subprocesses with following sequential two-body decays are considered:

$$(1) \psi(3686) \rightarrow \gamma + \chi_{c1}, \quad \chi_{c1} \rightarrow \eta' + f_0(X)/f_2(X), \\ f_0(X)/f_2(X) \rightarrow K^+ K^-;$$

(2) $\psi(3686) \rightarrow \gamma + \chi_{c1}, \chi_{c1} \rightarrow K_X^{*\pm} + K^\mp, K_X^{*\pm} \rightarrow \eta' K^\pm$. The two-body decay amplitudes are constructed in the covariant tensor formalism [18], and the radius of the centrifugal barrier is set to be 1.0 fm. Due to limited statistics in the fit, the line shape of intermediate states, e.g. $f_0(980)$, $f_0(1710)$, $f_2'(1525)$ and $K_X^{*\pm}(1430)$ etc. are all taken from the literature and fixed in the fit. The shape of $f_0(980)$ is described with the Flatté formula [19]:

$$\frac{1}{M^2 - s - i(g_1 \rho_{\pi\pi} + g_2 \rho_{KK})}, \quad (9)$$

where s is the $K^+ K^-$ invariant mass squared, and $\rho_{\pi\pi}$ and ρ_{KK} are Lorentz invariant phase space (PHSP) factors, $g_{1,2}$ are coupling constants to the corresponding final state, and the parameters are fixed to values measured in BESII [20]: $M = 0.965 \text{ GeV}/c^2$, $g_1 = 0.165 \text{ GeV}^2/c^4$, and $g_2/g_1 = 4.21$. The $f_2'(1525)$ and $f_0(1710)$ are parametrized with the Breit-Wigner propagator with constant width:

$$BW(s) = \frac{1}{M_R^2 - s - iM_R \Gamma_R}, \quad (10)$$

where M_R and Γ_R are the mass and width of the resonances, respectively, and are fixed at PDG values [1]. The excited kaon states at the $\eta' K^\pm$ invariant mass threshold are parametrized with the Flatté formula:

$$\frac{1}{M^2 - s - i(g_1 \rho_{K\pi}(s) + g_2 \rho_{\eta'K}(s))}, \quad (11)$$

where s is the $\eta' K$ invariant mass squared, $\rho_{K\pi}$ and $\rho_{\eta'K}$ are Lorentz invariant PHSP factors, and $g_{1,2}$ are coupling constants to the corresponding final state. The parameters of $K_0^{*\pm}(1430)$ are fixed to values measured by CLEO [5]:

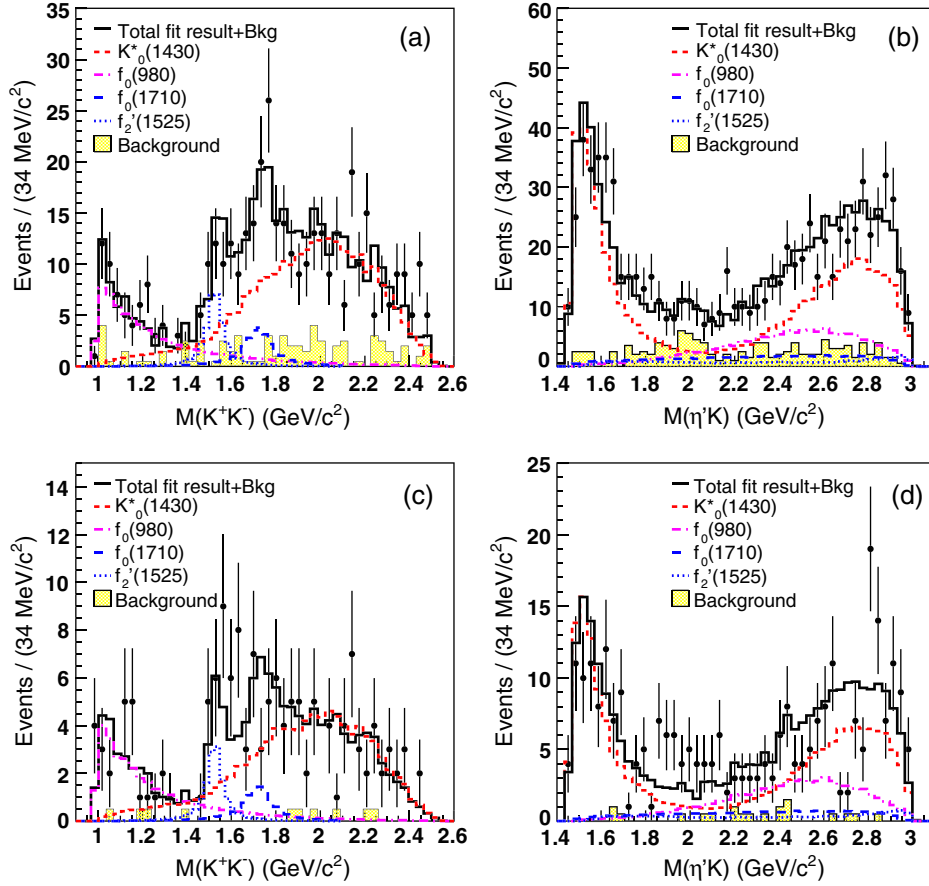


FIG. 8 (color online). The invariant mass distributions of K^+K^- and $\eta'K^\pm$ within the χ_{c1} mass range. (a),(b) for the η' decay mode I, and (c),(d) for the η' decay mode II.

$M = 1.4712 \text{ GeV}/c^2$, $g_1 = 0.2990 \text{ GeV}^2/c^4$, and $g_2 = 0.0529 \text{ GeV}^2/c^4$.

The decay amplitude is constructed as follows [18]:

$$A = \psi_\mu(m_1)e_\nu^*(m_2)A^{\mu\nu} = \psi_\mu(m_1)e_\nu^*(m_2) \sum_{i=1,2} \Lambda_{ij}U_{ij}^{\mu\nu}, \quad (12)$$

$$\Lambda_{ij} = \rho_{ij}e^{i\phi_{ij}} (j = 1, 2, \phi_{i1} = \phi_{i2}), \quad (13)$$

$$U_{ij}^{\mu\nu} = BW_{\chi_{cJ}} \times BW_i \times A_{ij}(J^{PC}), \quad (14)$$

where $\psi_\mu(m_1)$ is the polarization vector of $\psi(3686)$, $e_\nu(m_2)$ is the photon polarization vector, and $U_{ij}^{\mu\nu}$ is the amplitude of the i th state. For $\psi(3686) \rightarrow \gamma + \chi_{c1}$, $\chi_{c1} \rightarrow \eta' + X_i/K^\pm + X_i$, each intermediate state X_i will introduce two independent amplitudes, which are identified by the subscript $j = 1, 2$. The detailed formulas for $U_{ij}^{\mu\nu}$ for states with different J^{PC} , which are the same as those for $\psi \rightarrow \gamma\eta\pi^+\pi^-$, can be found in Ref. [18]. ρ_{ij} is the magnitude and ϕ_{ij} is the phase angle of the amplitude of the i th state. In the fit, the phase of the two amplitudes of

the same states are set to be same, $\phi_{i1} = \phi_{i2}$. $BW_{\chi_{cJ}}$ and BW_i are the propagators for χ_{cJ} and the intermediate states observed in the K^+K^- or $\eta'K^\pm$ invariant mass spectra, respectively. $A_{ij}(J^{PC})$ is the remaining part that is dependent on the J^{PC} of the intermediate states. Since all the parameters in the propagators are fixed in the fit, there are three free parameters (two magnitudes and one phase) for each state in the fit. The total differential cross section $d\sigma/d\phi$ is

$$\frac{d\sigma}{d\phi} = \frac{1}{2} \sum_{m_1=1}^2 \sum_{m_2=1}^2 \psi_\mu(m_1)e_\nu^*(m_2)A^{\mu\nu}\psi_{\mu'}^*(m_1)e_{\nu'}(m_2)A^{*\mu'\nu'}. \quad (15)$$

The relative magnitudes and phases of each subprocess are determined by an unbinned maximum likelihood fit. The probability to observe the event characterized by the measurement ξ_i is the differential cross section normalized to unity:

$$P(\xi_i, \alpha) = \frac{\omega(\xi_i, \alpha)\epsilon(\xi_i)}{\int d\xi_i \omega(\xi_i, \alpha)\epsilon(\xi_i)}, \quad (16)$$

where $\omega(\xi_i, \alpha) \equiv \left(\frac{d\sigma}{d\Omega}\right)_i$, α is a set of unknown parameters to be determined in the fitting, and $\epsilon(\xi_i)$ is the detection efficiency. The joint probability density for observing N events in the data sample is

$$\mathcal{L} = \prod_{i=1}^N P(\xi_i, \alpha) = \prod_{i=1}^N \frac{\omega(\xi_i, \alpha)\epsilon(\xi_i)}{\int d\xi_i \omega(\xi_i, \alpha)\epsilon(\xi_i)}. \quad (17)$$

FUMILI [21] is used to optimize the fit parameters to achieve the maximum likelihood value. Technically, rather than maximizing \mathcal{L} , $S = -\ln \mathcal{L}$ is minimized, i.e.,

$$S = -\ln \mathcal{L} = -\sum_{i=1}^N \ln \left(\frac{\omega(\xi_i, \alpha)}{\int d\xi_i \omega(\xi_i, \alpha)\epsilon(\xi_i)} \right) - \sum_{i=1}^N \ln \epsilon(\xi_i). \quad (18)$$

For a given data set, the second term is a constant and has no impact on the relative changes of the S value. In practice, the normalized integral $\int d\xi_i \omega(\xi_i, \alpha)\epsilon(\xi_i)$ is evaluated by the PHSP MC samples. The details of the PWA fit process are described in Ref. [22].

B. Background treatment

In this analysis, background contamination in the signal region is estimated from events within different sideband regions. The η' signal region is defined with the requirement (I) $|M(\gamma\pi^+\pi^-) - M(\eta')| < 15 \text{ MeV}/c^2$ for mode I, or $|M(\gamma\gamma\pi^+\pi^-) - M(\eta')| < 25 \text{ MeV}/c^2$ for mode II. While the η' sideband region is defined with the requirement (II) $20 \text{ MeV}/c^2 < |M(\gamma\pi^+\pi^-) - M(\eta')| < 50 \text{ MeV}/c^2$ or $30 \text{ MeV}/c^2 < |M(\gamma\gamma\pi^+\pi^-) - M(\eta')| < 80 \text{ MeV}/c^2$, respectively. The χ_{c1} signal region is defined with the requirement (III) $|M(\gamma\pi^+\pi^-K^+K^-) - M(\chi_{c1})| < 15 \text{ MeV}/c^2$ or $|M(\gamma\gamma\pi^+\pi^-K^+K^-) - M(\chi_{c1})| < 18 \text{ MeV}/c^2$ for the two η' decay modes, respectively. The χ_{c1} sideband region is

defined with requirement (IV) $20 \text{ MeV}/c^2 < M(\chi_{c1}) - M(\gamma\pi^+\pi^-K^+K^-) < 50 \text{ MeV}/c^2$ or $23 \text{ MeV}/c^2 < M(\chi_{c1}) - M(\gamma\gamma\pi^+\pi^-K^+K^-) < 59 \text{ MeV}/c^2$ for modes I and II, respectively.

In the PWA, χ_{c1} signal candidate events are selected with requirements I and III (box 0 in Fig. 9). The first category of background is the peaking $\gamma(\gamma)\pi^+\pi^-K^+K^-$ background in the χ_{c1} region, which is mainly from decay processes with the same final states, or with one more (less) photon in the final state, but without an η' , the non- η' background. This category of background can be estimated with events within the η' sideband region with requirements II and III (boxes 1 in Fig. 9). The second category of background is the nonpeaking background, the non- χ_{c1} background, which is mainly from direct $\psi(3686)$ radiative decay, $\psi(3686) \rightarrow \gamma\eta'K^+K^-$. This background can be estimated with the events within the χ_{c1} sideband region with requirements I and IV (box 2 in Fig. 9). There are also backgrounds from processes without χ_{c1} and η' intermediate states, the non- η' non- χ_{c1} background, which can be estimated with events with requirements II and IV (boxes 3 in Fig. 9). In the fit, background contributions to the log likelihood are estimated from the weighted events in the sideband regions, and subtracted in the fit, as following:

$$S = S_{\text{sig}} - \omega_{\text{bkg1}} \times S_{\text{bkg1}} - \omega_{\text{bkg2}} \times S_{\text{bkg2}} + \omega_{\text{bkg3}} \times S_{\text{bkg3}}$$

$$= -\sum_{i=1}^{N_{\text{sig}}} \ln \left(\frac{\omega(\xi_i^k, \alpha)}{\int d\xi_i \omega(\xi_i^k, \alpha)\epsilon(\xi_i)} \right)$$

$$+ \omega_{\text{bkg1}} \times \sum_{i=1}^{N_{\text{bkg1}}} \ln \left(\frac{\omega(\xi_i^k, \alpha)}{\int d\xi_i \omega(\xi_i^k, \alpha)\epsilon(\xi_i)} \right)$$

$$+ \omega_{\text{bkg2}} \times \sum_{i=1}^{N_{\text{bkg2}}} \ln \left(\frac{\omega(\xi_i^k, \alpha)}{\int d\xi_i \omega(\xi_i^k, \alpha)\epsilon(\xi_i)} \right)$$

$$- \omega_{\text{bkg3}} \times \sum_{i=1}^{N_{\text{bkg3}}} \ln \left(\frac{\omega(\xi_i^k, \alpha)}{\int d\xi_i \omega(\xi_i^k, \alpha)\epsilon(\xi_i)} \right), \quad (19)$$

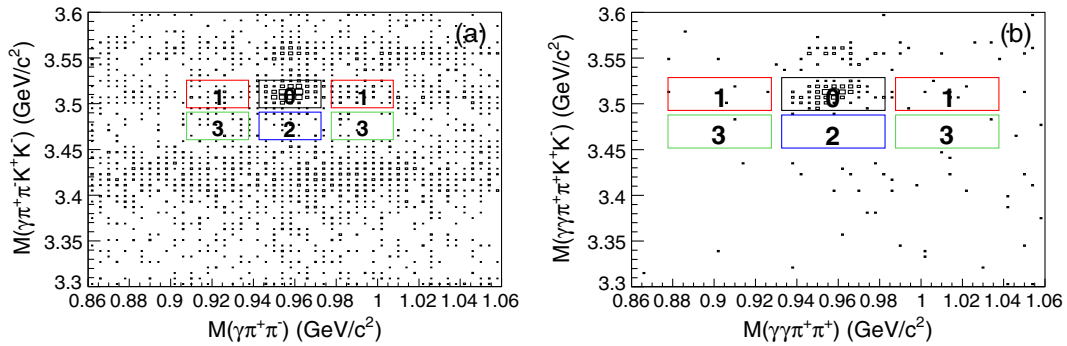


FIG. 9 (color online). (a) The scatter plot of $M(\gamma\pi^+\pi^-K^+K^-)$ versus $M(\gamma\pi^+\pi^-)$ for mode I. (b) The scatter plot of $M(\gamma\gamma\pi^+\pi^-K^+K^-)$ versus $M(\gamma\gamma\pi^+\pi^-)$ for mode II. The plots here are the zoom-in subregions of Fig. 3(a) and Fig. 4(a) around η' and χ_{cJ} . The boxes defining the signal and sideband regions are described in the text.

where N_{sig} , N_{bkg1} , N_{bkg2} and N_{bkg3} are the numbers of events in the signal regions, non- η' , non- χ_{c1} and non- η' non- χ_{c1} sideband regions, respectively. The ω_{bkg1} , ω_{bkg2} , and ω_{bkg3} are the normalization weights of events in different sideband regions, and are taken to be 0.5, 1.0, 0.5 in the fit, respectively. The sign before ω_{bkg3} is different with ω_{bkg1} and ω_{bkg2} because the third category of background is double counted in the first two categories of background.

C. PWA procedure and result

To improve the sensitivity for each subprocess, a combined fit on the candidate events of the two η' decay modes is carried out, and the combined log likelihood value:

$$S_{\text{total}} = S_1 + S_2 = -\ln \mathcal{L}_1 - \ln \mathcal{L}_2 \quad (20)$$

is used to optimize the fit parameters. Here, S_1 and S_2 are the log likelihoods of the two decay modes, respectively. In the fitting, two individual PHSP MC samples [$\psi(3686) \rightarrow \gamma\chi_{c1}, \chi_{c1} \rightarrow \eta' K^+ K^-$, $\eta' \rightarrow \gamma\rho^0$ or $\eta' \rightarrow \eta\pi^+\pi^-$] are generated for the normalized integral of the two η' decay modes, respectively. Since the χ_{cJ} signal is included in the MC samples, the propagator of $BW_{\chi_{cJ}}$ in Eq. (14) is set to be unity in the fit.

Different combinations of states of $f_{0,2}(x)$, $K_{0,1,2}^*(x)$ have been tested. Because of the limited statistics, only the well-established states in the PDG with statistical significance larger than 5σ are included in the nominal result.

Some different assumptions of the intermediate states are considered and will be described in detail in Sec. VIII E. Finally, only four intermediate states, $f_0(980)$, $f_0(1710)$, $f_2'(1525)$ and $K_0^*(1430)$, are included in the nominal result.

The $M(K^+K^-)$ and $M(\gamma(\gamma)\pi^+\pi^-K^\pm)$ distributions of data and the PWA fit projections, as well as the contributions of individual subprocesses for the optimal solution are shown in Fig. 8 for the two η' decay modes. The corresponding comparisons of angular distributions $\theta(X-Y)$, the polar angle of particle X in Y -helicity frame, are shown in Fig. 10. The PWA fit projection is the sum of the signal contribution of the best solution and the backgrounds estimated with the events within the sideband regions. The Dalitz plots of data and MC projection from the best solution of the PWA for the two η' decays modes are shown in Fig. 11.

To determine goodness of the fit, a χ^2 is calculated by comparing data and the fit projection histograms, where χ^2 is defined as

$$\chi^2 = \sum_{i=1}^r \frac{(n_i - v_i)^2}{v_i}. \quad (21)$$

Here n_i and v_i are the number of events for data and the fit projections in the i th bin of each figure, respectively. If v_i of one bin is less than five, the bin is merged to the neighboring bin with the smaller bin content. The corresponding χ^2 and the number of bins of each mass and angular distributions for the two η' decay modes as well as

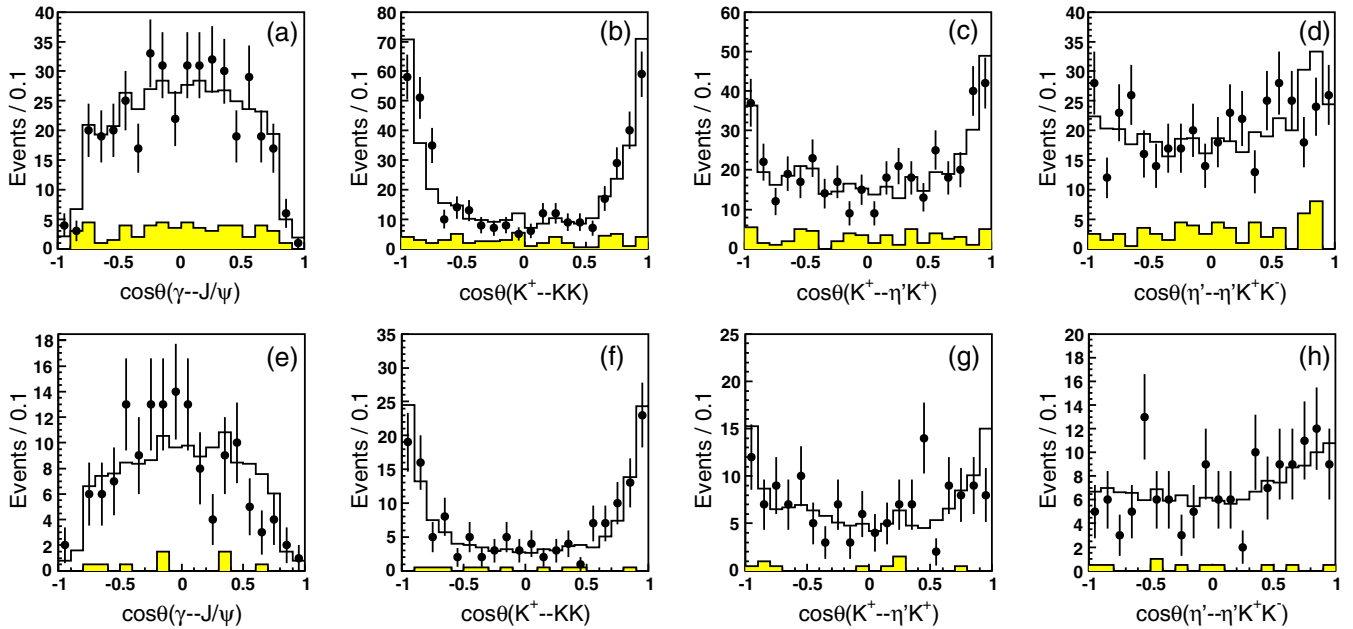


FIG. 10 (color online). Comparisons of angular distributions $\cos\theta(\gamma - J/\psi)$, $\cos\theta(K^+ - K^+K^-)$, $\cos\theta(K^+ - \eta'K^+)$, $\cos\theta(\eta' - \eta'K^+K^-)$, (a), (b), (c), (d) for the η' decay mode I, (e), (f), (g), (h) for the η' decay mode II. The empty histogram shows the global fit result combined with the background contribution. The filled histogram shows background.

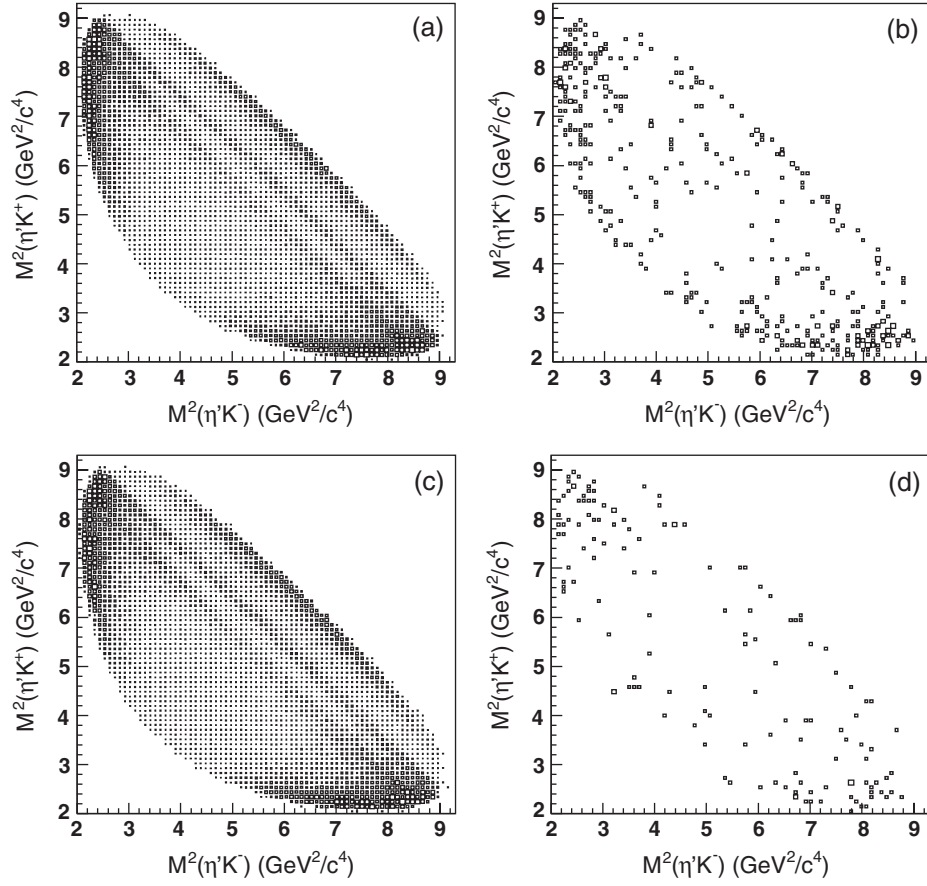


FIG. 11. Dalitz plots of $M^2(\eta'K^+)$ versus $M^2(\eta'K^-)$. (a) of MC projections for the η' decay mode I; (b) of data for the η' decay mode I; (c) of MC projections for the η' decay mode II; and (d) of data for the η' decay mode II.

for the combined distributions are shown in Table III. The values of $\chi^2/(N_{\text{bin}} - 1)$ of combined distributions are between 0.67 and 1.52, indicating reasonable agreement between data and the fit projection.

D. Partial Branching fraction measurements

To get the branching fractions of individual subprocesses with sequential two-body decay, the cross section fraction of the i th subprocess is calculated with MC integral method:

$$F_i = \frac{\sum_{j=1}^{N_{mc}} \left(\frac{d\sigma}{d\phi}\right)_j^i}{\sum_{j=1}^{N_{mc}} \left(\frac{d\sigma}{d\phi}\right)_j}. \quad (22)$$

In practice, a large PHSP MC sample without any selection requirements is used to calculate F_i , where $\left(\frac{d\sigma}{d\phi}\right)_j^i$ and $\left(\frac{d\sigma}{d\phi}\right)_j$ are the differential cross section of the i th subprocess and the total differential cross section for the j th MC event, and N_{mc} is the total number of MC events.

The statistical uncertainties of the magnitudes, phases and F_i are estimated with a bootstrap method [23]. 300 new samples are formed by random sampling from the original data set, each with equal size as the original. All the

samples are subjected to the same analysis as the original sample. The statistical uncertainties of the magnitudes, phases and F_i are the standard deviations of the corresponding distributions obtained and are listed in Table IV.

The partial branching fraction of the i th subprocess is

$$\mathcal{B}_i = \mathcal{B}(\chi_{cJ} \rightarrow \eta'K^+K^-) \times F_i \quad (23)$$

where $\mathcal{B}(\chi_{cJ} \rightarrow \eta'K^+K^-)$ is the average branching fraction in Table IX. The corresponding statistical uncertainty of \mathcal{B}_i contains two parts: one is from the statistical uncertainty of $\mathcal{B}(\chi_{cJ} \rightarrow \eta'K^+K^-)$ (σ_1), and the other part is from the statistical uncertainty of F_i (σ_2).

$$\begin{aligned} \sigma_1 &= \sigma(\mathcal{B}(\chi_{cJ} \rightarrow \eta'K^+K^-)) \times F_i, \\ \sigma_2 &= \mathcal{B}(\chi_{cJ} \rightarrow \eta'K^+K^-) \times \sigma(F_i). \end{aligned} \quad (24)$$

The statistical uncertainty of $\mathcal{B}(\chi_{cJ} \rightarrow \eta'K^+K^-)$ is calculated with a weighted χ^2 method:

$$\sigma(\mathcal{B}(\chi_{cJ} \rightarrow \eta'K^+K^-)) = \sqrt{\frac{\sigma_{s1}^2 \sigma_{s2}^2}{\sigma_{s1}^2 + \sigma_{s2}^2}}, \quad (25)$$

TABLE III. Goodness of fit check for the invariant mass and angular distributions.

	Variable	$M_{K^+K^-}$	$M_{\eta'K}$	$\theta_{\gamma-J\psi}$	θ_{K^+-KK}	$\theta_{K^+-\eta'K^+}$	$\theta_{\eta'-\eta'K^+K^-}$
$\eta' \rightarrow \gamma\rho^0$	χ^2	56.6	47.8	10.8	34.4	20.1	29.2
	N_{bin}	37	46	18	20	20	20
	$\chi^2/(N_{\text{bin}} - 1)$	1.57	1.06	0.63	1.81	1.06	1.54
$\eta' \rightarrow \eta\pi^+\pi^-$	χ^2	23.7	74.3	17.0	6.6	27.0	20.4
	N_{bin}	20	33	16	14	17	20
	$\chi^2/(N_{\text{bin}} - 1)$	1.25	2.32	1.13	0.51	1.69	1.07
Combine	χ^2	56.3	59.9	11.4	27.2	20.7	17.7
	N_{bin}	38	46	18	20	20	20
	$\chi^2/(N_{\text{bin}} - 1)$	1.52	1.33	0.67	1.43	1.09	0.93

TABLE IV. The fitted magnitudes, phases, fractions and the corresponding partial branching fractions of individual processes in the nominal fit (statistical uncertainties only).

Process	Magnitude	Magnitude	Phase	Fraction	Partial branching fraction
	ρ_{i1}	ρ_{i2}	$\phi_{i1} = \phi_{i2}$ (rad)	F_i (%)	$\mathcal{B}(10^{-4})$
$\chi_{c1} \rightarrow K_0^*(1430)^\pm K^\mp, K_0^*(1430)^\pm \rightarrow \eta' K^\pm$	1 (Fixed)	0.13 ± 0.11	0 (Fixed)	73.26 ± 5.03	6.41 ± 0.57
$\chi_{c1} \rightarrow \eta' f_0(980), f_0(980) \rightarrow K^+ K^-$	0.77 ± 0.11	0.12 ± 0.16	5.50 ± 0.28	18.90 ± 5.26	1.65 ± 0.47
$\chi_{c1} \rightarrow \eta' f_0(1710), f_0(1710) \rightarrow K^+ K^-$	0.88 ± 0.20	0.03 ± 0.30	0.96 ± 0.18	8.11 ± 2.43	0.71 ± 0.22
$\chi_{c1} \rightarrow \eta' f_2'(1525), f_2'(1525) \rightarrow K^+ K^-$	-0.17 ± 0.03	0.01 ± 0.05	6.02 ± 0.21	10.50 ± 2.63	0.92 ± 0.23

where σ_{s1} and σ_{s2} are the statistical uncertainties given by the two decay modes listed in Table IX. Finally the total statistical uncertainty of the i th subprocess is

$$\sigma(\mathcal{B}_i) = \sqrt{\sigma_1^2 + \sigma_2^2}. \quad (26)$$

The results of cross section fraction F_i and the partial branching fractions of individual subprocesses as well as the two independent magnitudes and phase of each state of the baseline fit are shown in Table IV, where only statistical uncertainties are listed.

E. Checks for the best solution

Various alternative PWA fits with different assumptions are carried out to check the reliability of the results. To get the statistical significance of individual subprocesses, alternative fits with dropping one given subprocess are performed. The changes of log likelihood value $\Delta\mathcal{S}$ and of the number of degrees of freedom $\Delta ndof$ as well as the corresponding statistical significance are listed in Table V. Each subprocess has a statistical significance larger than 5σ .

To determine the spin parity of each intermediate state, alternative fits with different spin-parity hypotheses of the $K_X^{*\pm}(1430)$, $f_X(1710)$ and $f_X(1525)$ are performed. If J^P of $K_X^{*\pm}(1430)$ is replaced with 1^- or 2^+ , the log likelihood value is increased by 35 or 99, respectively. If J^P of $f_X(1525)$ is replaced with 0^{++} , the log likelihood value is increased by 12, while it increases by 7.4 when using the

mass and width of the $f_0(1500)$ in the fit. If J^P of $f_X(1710)$ is replaced with 2^{++} , the log likelihood value is improved by 1.3, so there is some ambiguity for the J^P of the $f_X(1710)$ due to small statistics. Since there is no known meson with $J^P = 2^{++}$ around $1.7 \text{ GeV}/c^2$ in PDG, the structure around $1.7 \text{ GeV}/c^2$ in K^+K^- invariant mass is assigned to be $f_0(1710)$ in the analysis. In the above tests, the mass and width of each intermediate states are fixed to PDG values in the fit [1]. If we scan the mass and width of all the states, $M(f_X(1710)) \simeq 1.705 \text{ GeV}/c^2$ and $\Gamma(f_X(1710)) \simeq 0.1331 \text{ GeV}/c^2$, which agree well with the PDG values, and the spin parity of $f_X(1710)$ favors 0^{++} over 2^{++} with log likelihood value improved by 11.

To check the contributions from other possible subprocesses, alternative fits with additional known mesons listed in the PDG are carried out. Under spin-parity constraints, the intermediate mesons $f_2(1270)$, $f_0(1370)$, $f_0(1500)$, $f_2(1910)$, $f_2(1950)$, $f_2(2010)$, $f_0(2020)$, $f_0(2100)$, and $f_2(2150)$ decaying to K^+K^- , as well as $K_1^*(1410)$, $K_2^*(1430)$ and $K_1^*(1680)$ decaying to $\eta'K^\pm$ are included in the fit individually, and the masses and widths of these intermediate states are fixed to values in the PDG. For $f_0(1370)$, there is no average value in PDG, so its mass and width are fixed to the middle value of the PDG range, $M = 1.35 \text{ GeV}/c^2$, $\Gamma = 0.35 \text{ GeV}/c^2$. To investigate the contribution from the direct $\chi_{c1} \rightarrow \eta'K^+K^-$ decay (PHSP), two fits with different PHSP approximations are carried out, where the first assumes that the K^+K^- system is a very broad state with $J^P = 0^{++}$, and the other assumes that the

TABLE V. Change in the log likelihood value $\Delta\mathcal{S}$, associated change of degrees of freedom $\Delta ndof$, and statistical significance if a process is dropped from the fit.

Process	$\chi_{c1} \rightarrow K_0^*(1430)K$	$\chi_{c1} \rightarrow f_0(980)\eta'$	$\chi_{c1} \rightarrow f_0(1710)\eta'$	$\chi_{c1} \rightarrow f_2'(1525)\eta'$
$\Delta\mathcal{S}$	323	89.7	22.8	33.2
$\Delta ndof$	3	3	3	3
Significance	$\gg 8\sigma$	$\gg 8\sigma$	6.2σ	7.6σ

TABLE VI. The change of log likelihood value $\Delta\mathcal{S}$, of the number of freedom $\Delta ndof$ and the corresponding significance with additional processes on K^+K^- invariant mass spectrum, where PHSP₁ represent for PHSP with K^+K^- broad states.

Add. res.	$f_2(1270)$	$f_0(1370)$	$f_0(1500)$	$f_2(1910)$	$f_2(1950)$	$f_2(2010)$	$f_0(2020)$	$f_0(2100)$	$f_2(2150)$	PHSP ₁
$\Delta\mathcal{S}$	6.0	10.2	6.7	5.0	5.9	5.1	15.4	18.0	7.3	15.0
$\Delta ndof$	3	3	3	3	3	3	3	3	3	3
Significance	2.7σ	3.8σ	2.9σ	2.4σ	2.6σ	2.4σ	4.9σ	5.4σ	3.1σ	4.8σ

$\eta'K^\pm$ system is a very broad state with $J^P = 0^+$. The likelihood value change $\Delta\mathcal{S}$, the number of freedom change $\Delta ndof$ as well as the corresponding significance of various additional subprocesses are summarized in Table VI and Table VII. The subprocesses with an intermediate state of $f_0(2100)$, $K_2^*(1430)$ and $K_1^*(1680)$ have significances larger than 5σ . $f_0(2020)$ has a significance of 4.9σ . There might be some f_0 states around $2.1\text{ GeV}/c^2$, but they are not as well established as $f_0(1710)$ and $f_2'(1525)$, and it is impossible to tell which might be here. Because they are far from $f_0(1710)$ and should have little interference with other resonances, we did not include any f_0 state around $2.1\text{ GeV}/c^2$ in nominal result. Their possible influence will be considered in the systematic uncertainty. For $K_2^*(1430)$ and $K_1^*(1680)$, the large significance mainly comes from the imperfect fit to real data with the $K_0^*(1430)$ line shape cited. If we scan the mass and width of intermediate states in the fit instead of fixing them, the fit result agrees better with data and the significances of the $K_2^*(1430)$ and $K_1^*(1680)$ are only 0.6σ and 3.4σ , respectively. It is therefore difficult to confirm the existence of $K_2^*(1430)$ and $K_1^*(1680)$ decays to $K\eta'$ with the available data, and these subprocesses are not included in the nominal solution. The influence on the measurement of these states is considered in the systematic uncertainty. The fit results obtained using resonance parameters from the

mass and width scans are also taken into account in the systematic uncertainty.

F. The systematic uncertainty

Several sources of systematic uncertainty are considered in determination of the individual partial branching fractions:

- The value of the centrifugal barrier R:* In the fit, centrifugal barrier R is 1.0 fm. Alternative PWA fits with R varied from 0.1 to 1.5 fm are performed. The differences of partial branching fractions from the nominal results are taken as the systematic uncertainties from the centrifugal barrier.
- The uncertainty from additional states:* As mentioned above, there are possible contributions from other subprocesses with different intermediate states in $\chi_{c1} \rightarrow \eta'K^+K^-$ decay. Several alternative fits including known states listed in the PDG and the two different approximations of PHSP are carried out, and the largest differences of partial branching fractions are taken as the systematic uncertainties.
- The shape of $K_0^*(1430)$:* Because $K_0^*(1430)$ is at the $\eta'K^\pm$ threshold, the Flatté formula [Eq. (11)] is used to parametrize the shape of $K_0^*(1430)$ in nominal fit. A PWA with an alternative Flatté formula:

$$f(s) = \frac{1}{M^2 - s - iM\Gamma(s)},$$

$$\Gamma(s) = \frac{s - s_A}{M^2 - s_A} \cdot g_1^2 \cdot \rho_{K\pi}(s) + \frac{s - s_A}{M^2 - s_A} \cdot g_2^2 \cdot \rho_{K\eta}(s),$$
(27)

TABLE VII. The change of log likelihood value $\Delta\mathcal{S}$, of the number of freedom $\Delta ndof$ and the corresponding significance with additional processes on $\eta'K$ invariant mass spectrum, where PHSP₂ represent for PHSP with $\eta'K$ broad states.

Add. res.	$K_1^*(1410)$	$K_2^*(1430)$	$K_1^*(1680)$	PHSP ₂
$\Delta\mathcal{S}$	11.1	27.6	19	15.0
$\Delta ndof$	3	3	3	3
Significance	4.0σ	6.8σ	5.7σ	4.8σ

for $K_0^*(1430)$ is performed. Here $M = 1.517\text{ GeV}/c^2$, the Adler zero $s_A = m_K^2 - m_\pi^2/2 \approx 0.23\text{ GeV}^2/c^4$, $g_1^2 = 0.353\text{ GeV}/c^2$, and $g_2^2/g_1^2 = 1.15$, are from Ref. [6]. As mentioned at the end of Sec. VIII E,

TABLE VIII. Summary for systematic uncertainties of partial branching fraction of intermediate states (in %).

	$K_0^*(1430)$	$f_0(980)$	$f_0(1710)$	$f_2'(1525)$
The R Value	+2.0 -9.1	+12.6 -12.0	+18.0 -23.6	+12.9 -28.0
The additional states	+22.2 -40.4	+58.7 -25.7	+93.1 -54.2	+51.6 -39.8
The shape of $K_0^*(1430)$	+22.2 -0	+52.1 -0	+0 -26.4	+26.1 -0
The background	+0 -0.2	+0 -16.7	+0 -15.5	+0 -23.9
Mass and width uncertainty on PDG	+1.4 -0.9	+4.8 -1.8	+4.2 -4.2	+2.2 -1.1
$\mathcal{B}(\chi_{cJ} \rightarrow \eta' K^+ K^-)$	+8.6 -8.6	+8.6 -8.6	+8.6 -8.6	+8.6 -8.6
Total	+32.6 -42.3	+80.1 -34.1	+95.3 -67.3	+59.9 -54.9

the fit result using resonance parameters from the mass and width scans are also considered. The largest differences of the partial branching fractions to the nominal values are taken as the systematic uncertainties associated with the $K_0^*(1430)$ parametrization.

- (d) *The mass and width uncertainties of intermediate states:* As mentioned in Sec. VIII A, the mass and width of intermediate states, i.e. $f_0(1710)$, $f_2'(1525)$ and $K_0^*(1430)$ are fixed to the values in the PDG or in the corresponding literature. PWA fits with changes in

the masses and widths of intermediate states by 1σ are performed individually. The largest differences on the partial branching fractions are taken as the systematic uncertainties.

- (e) *Background uncertainty:* To estimate the systematic uncertainty from background, alternative intervals of sideband regions are defined, and the PWA fit is redone. The differences to the nominal partial branching fractions are taken as the systematic uncertainties.
- (f) The uncertainty from $\mathcal{B}(\chi_{c1} \rightarrow \eta' K^+ K^-)$: Because the total branching fraction $\mathcal{B}(\chi_{cJ} \rightarrow \eta' K^+ K^-)$ is used to calculate the individual partial branching fractions of intermediate states, the systematic uncertainty of $\mathcal{B}(\chi_{cJ} \rightarrow \eta' K^+ K^-)$, 0.75×10^{-4} , must be included.

A summary of the partial branching fraction systematic uncertainties for individual subprocesses are shown in Table VIII. The total systematic uncertainties are obtained by adding the individual contributions in quadrature.

IX. PWA FOR χ_{c2}

Figure 12 shows the $M(K^+K^-)$ and $M(\gamma(\gamma)\pi^+\pi^-K^\pm)$ distributions after the χ_{c2} mass window requirement:

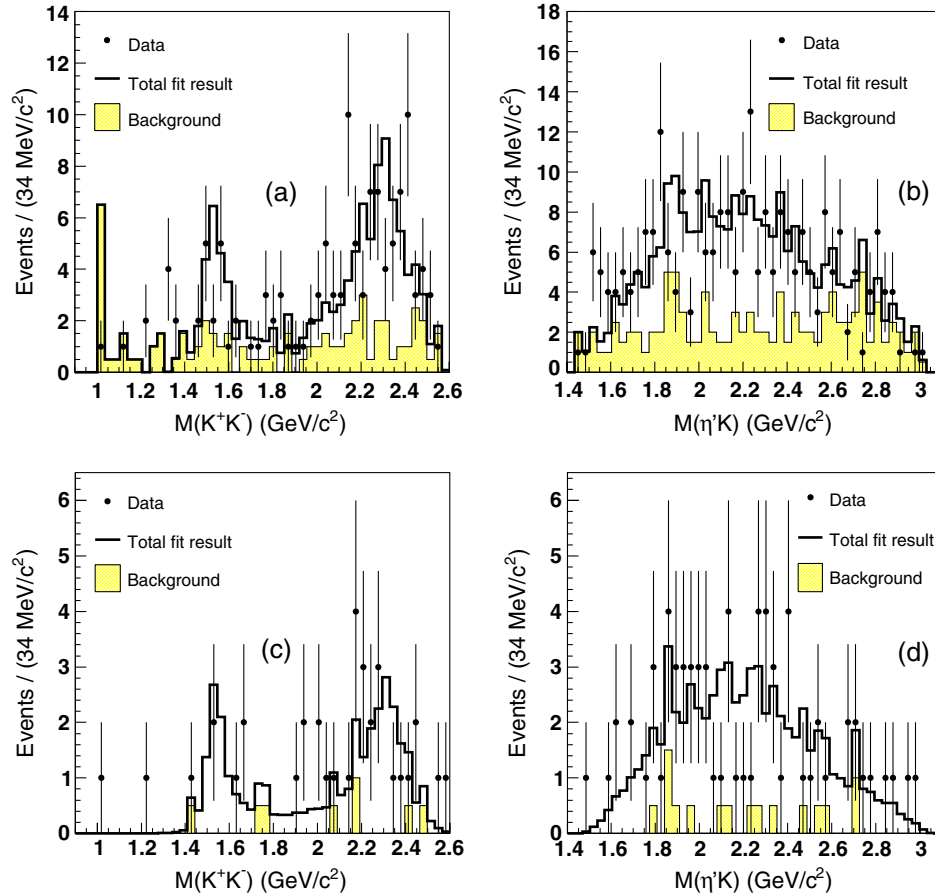


FIG. 12 (color online). The invariant mass distributions of K^+K^- and $\gamma(\gamma)\pi^+\pi^-K^\pm$ for events within the χ_{c2} selection range. (a),(b) for the η' decay mode I, and (c),(d) for the η' decay mode II.

TABLE IX. The branching fractions of $\chi_{c1,2} \rightarrow \eta' K^+ K^-$ and partial branching fractions of χ_{c1} decay to intermediate states. The first uncertainties are statistical, and the second are systematic. For the average branching fraction, the uncertainty is the combined uncertainty.

Process		$\mathcal{B}(\times 10^{-4})$
$\mathcal{B}(\chi_{c1} \rightarrow \eta' K^+ K^-)$	$\eta' \rightarrow \gamma \rho^0$	$9.09 \pm 0.54 \pm 0.86$
	$\eta' \rightarrow \eta \pi^+ \pi^-$	$8.33 \pm 0.77 \pm 0.77$
	average	8.75 ± 0.87
$\mathcal{B}(\chi_{c2} \rightarrow \eta' K^+ K^-)$	$\eta' \rightarrow \gamma \rho^0$	$1.84 \pm 0.31 \pm 0.33$
	$\eta' \rightarrow \eta \pi^+ \pi^-$	$2.05 \pm 0.41 \pm 0.25$
	average	1.94 ± 0.34
$\chi_{c1} \rightarrow K_0^*(1430)^\pm K^\mp, K_0^*(1430)^\pm \rightarrow \eta' K^\pm$		$6.41 \pm 0.57_{-2.71}^{+2.09}$
$\chi_{c1} \rightarrow \eta' f_0(980), f_0(980) \rightarrow K^+ K^-$		$1.65 \pm 0.47_{-0.56}^{+1.32}$
$\chi_{c1} \rightarrow \eta' f_0(1710), f_0(1710) \rightarrow K^+ K^-$		$0.71 \pm 0.22_{-0.48}^{+0.68}$
$\chi_{c1} \rightarrow \eta' f_2'(1525), f_2'(1525) \rightarrow K^+ K^-$		$0.92 \pm 0.23_{-0.51}^{+0.55}$

$|M(\gamma \pi^+ \pi^- K^+ K^-) - M(\chi_{c2})| < 16 \text{ MeV}/c^2$ for mode I and $|M(\gamma \gamma \pi^+ \pi^- K^+ K^-) - M(\chi_{c2})| < 18 \text{ MeV}/c^2$ for mode II. There is a small structure around $1.5 \text{ GeV}/c^2$ and a very wide structure around $2.3 \text{ GeV}/c^2$ in the $K^+ K^-$ invariant mass spectrum. No obvious structure is observed in the $\eta' K^\pm$ invariant mass spectrum. From spin-parity conservation, the decays $\chi_{c2} \rightarrow f_0 \eta'$ and $\chi_{c2} \rightarrow K_0^{\pm} K^\mp$ are forbidden. A possible process is $\chi_{c2} \rightarrow f_2 \eta'$. Since there are few events and the background is about 50%, estimated by fitting of $\eta' K^+ K^-$ invariant mass distribution, a simple simultaneous PWA fit is performed on the candidate events of the two η' decay modes. No intermediate state results are given; the PWA is only used to generate MC samples to determine the detection efficiency of $\chi_{c2} \rightarrow \eta' K^+ K^-$.

In the PWA, only $f_2'(1525)$ and $f_2(2300)$ states in the $K^+ K^-$ invariant mass distribution are considered. The mass and width of $f_2'(1525)$ are fixed to PDG values [1]. The mass and width of $f_2(2300)$ are about $2.323 \text{ GeV}/c^2$ and $0.183 \text{ GeV}/c^2$ from a rough scan. The PWA fit with or without background subtraction is performed, where the background is estimated from the η' sideband events. The difference of detection efficiency given for the two cases is taken as systematic uncertainty when measuring $\mathcal{B}(\chi_{c2} \rightarrow \eta' K^+ K^-)$.

X. SUMMARY

Based on a sample of $(106.41 \pm 0.86) \times 10^6 \psi(3686)$ events collected with the BESIII detector, the branching fractions of $\chi_{c1,2} \rightarrow \eta' K^+ K^-$ are measured with $\eta' \rightarrow \gamma \rho^0$ and $\eta' \rightarrow \eta \pi^+ \pi^-$. The measured branching fractions are summarized in Table IX. Abundant structures on the $K^+ K^-$ and $\eta' K^\pm$ invariant mass spectra are observed for χ_{c1} candidate events, and a simultaneous PWA with covariant tensor amplitudes is performed for the two η' decay modes. The partial branching fractions of χ_{c1} decay processes with intermediate states $f_0(980)$, $f_0(1710)$, $f_2'(1525)$ and

$K_0^*(1430)$ are measured and summarized in the Table IX. All of these branching fractions are measured for the first time. As mentioned in the Introduction, the results can be used to constrain glueball- $q\bar{q}$ mixing schemes for scalar mesons. However, both the theory in Ref. [4] and our measurement result has large uncertainty. Our result cannot distinguish between the mixing schemes. The decay $K_0^*(1430)^\pm \rightarrow \eta' K^\pm$ is observed for the first time.

ACKNOWLEDGMENTS

The BESIII Collaboration thanks the staff of BEPCII and the computing center for their strong support. This work is supported in part by the Ministry of Science and Technology of China under Contract No. 2009CB825200; Joint Funds of the National Natural Science Foundation of China under Contracts No. 11079008, No. 11179007, No. U1332201; National Natural Science Foundation of China (NSFC) under Contracts No. 10625524, No. 10821063, No. 10825524, No. 10835001, No. 10935007, No. 10979038, No. 11005109, No. 11079030, No. 11125525, No. 11235011, No. 11275189, No. 11322544, No. 11375204; the Chinese Academy of Sciences (CAS) Large-Scale Scientific Facility Program; CAS under Contracts No. KJCX2-YW-N29, No. KJCX2-YW-N45; 100 Talents Program of CAS; German Research Foundation DFG under Contract No. Collaborative Research Center CRC-1044; Istituto Nazionale di Fisica Nucleare, Italy; Ministry of Development of Turkey under Contract No. DPT2006 K-120470; U.S. Department of Energy under Contracts No. DE-FG02-04ER41291, No. DE-FG02-05ER41374, No. DE-FG02-94ER40823, No. DESC0010118; U.S. National Science Foundation; University of Groningen (RuG) and the Helmholtzzentrum fuer Schwerionenforschung GmbH (GSI), Darmstadt; WCU Program of National Research Foundation of Korea under Contract No. R32-2008-000-10155-0.

- [1] J. Beringer *et al.* (Particle Data Group), *Phys. Rev. D* **86**, 010001 (2012).
- [2] V. V. Anisovich, *Phys. Usp.* **41**, 419 (1998).
- [3] C. N. Yang, *Phys. Rev.* **77**, 242 (1950).
- [4] Q. Wang, G. Li, and Q. Zhao, *Int. J. Mod. Phys. A* **27**, 1250135 (2012).
- [5] G. Bonvicini *et al.* (CLEO Collaboration), *Phys. Rev. D* **78**, 052001 (2008).
- [6] D. V. Bugg, *Phys. Lett. B* **632**, 471 (2006).
- [7] M. Ablikim *et al.* (BESIII Collaboration), *Chin. Phys. C* **37**, 063001 (2013).
- [8] M. Ablikim *et al.* (BESIII Collaboration), *Nucl. Instrum. Methods Phys. Res., Sect. A* **614**, 345 (2010).
- [9] D. M. Asner *et al.*, *Int. J. Mod. Phys. A* **24**, 499 (2009).
- [10] Z. Y. Deng *et al.*, *High Energy Phys. Nucl. Phys.* **30**, 371 (2006).
- [11] S. Jadach, B. F. L. Ward, and Z. Was, *Comput. Phys. Commun.* **130**, 260 (2000); S. Jadach, B. F. L. Ward and Z. Was, *Phys. Rev. D* **63**, 113009 (2001).
- [12] R. G. Ping, *Chin. Phys. C* **32**, 599 (2008).
- [13] J. C. Chen, G. S. Huang, X. R. Qi, D. H. Zhang, and Y. S. Zhu, *Phys. Rev. D* **62**, 034003 (2000).
- [14] M. Ablikim *et al.* (BESIII Collaboration), *Phys. Rev. D* **83**, 012003 (2011).
- [15] M. Ablikim *et al.* (BESIII Collaboration), *Phys. Rev. D* **83**, 112005 (2011).
- [16] M. Ablikim *et al.* (BESIII Collaboration), *Phys. Rev. D* **85**, 092012 (2012).
- [17] G. D'Agostini, *Nucl. Instrum. Methods Phys. Res., Sect. A* **346**, 306 (1994).
- [18] B. S. Zou and D. V. Bugg, *Eur. Phys. J. A* **16**, 537 (2003).
- [19] S. M. Flatté, *Phys. Lett. B* **63**, 224 (1976).
- [20] M. Ablikim *et al.* (BES Collaboration), *Phys. Lett. B* **607**, 243 (2005).
- [21] I. N. Silin and S. N. Sokolov, CERN Program Library D **510** (1971), <http://wwwasdoc.web.cern.ch/wwwasdoc/shortwrupsdir/d510/top.html>.
- [22] M. Ablikim *et al.* (BES Collaboration), *Phys. Rev. D* **72**, 092002 (2005).
- [23] B. Efron and R. Tibshirani, *An Introduction to the Bootstrap* (Chapman & Hall/CRC, New York, 1993).